Periodic Models in Quantum Chemical Simulations of *F* Centers in Crystalline Metal Oxides

YURI F. ZHUKOVSKII,[1,2] EUGENE A. KOTOMIN,[1,2]
ROBERT A. EVARESTOV,[3] DONALD E. ELLIS[2]

[1]*Institute of Solid State Physics, University of Latvia, 8 Kengaraga Str., LV-1063 Riga, Latvia*
[2]*Materials Research Center, Northwestern University, 2145 Sheridan Rd., Evanston, IL 60208, USA*
[3]*Department of Quantum Chemistry, St. Petersburg State University, 26 Universitetskii Prosp. Stary Peterhof, 198504 St. Petersburg, Russia*

ABSTRACT: We present a survey of recent first principles simulations of the neutral oxygen vacancies (*F* centers) existing as native or radiation-induced point defects in various crystalline metal oxides in different forms (bulk, bare substrate surface, and on the interface with metal adsorbates). We mainly consider periodic models in calculations of point defects using the metal oxide supercell or cyclic clusters. We compare different formalisms of first principles calculations, mostly the Density Functional Theory (DFT) as implemented in the framework of either localized basis set of atomic orbitals or delocalized basis sets of plane waves. We analyze in detail the structural and electronic properties of *F* centers in binary oxides of light metals (MgO and Al_2O_3), and ternary metal oxides ($SrTiO_3$, $BaTiO_3$, $PbTiO_3$, $KNbO_3$, and $PbZrO_3$ perovskites). When available, we compare results of ab initio periodic defect calculations with experimental data, results of the first principles cluster calculations (both embedded and molecular) as well as with semi-empirical calculations.   © 2007 Wiley Periodicals, Inc. Int J Quantum Chem 107: 2956–2985, 2007

Key words: ab initio periodic calculations; binary and ternary metal oxides; bulk; bare substrate surfaces; metal/oxide interfaces; neutral *F* centers (oxygen vacancies); point defect formation and migration; electronic properties of defective metal oxides

1. Introduction

Beneficial properties of crystalline metal oxides could be obtained by a deliberate deviation of atom concentration from the ideal stoichiometry that is relevant for their numerous high-tech applications [1]. This can be achieved by thermal treatment or irradiation of these materials, which leads to the displacement of atoms from their lattice sites into interstitial positions with further diffusion leaving vacancies behind [2]. The largest theoretical attention in quantum chemical calculations was paid so far to electronic *F* centers (neutral oxygen vacancies), mainly due to their numerous optical applications and presence in all metal oxides [3]. There exist a number of books and reviews published recently dealing with defects, in particular the *F* centers in various oxides and how they affect host crystal properties [1–9]. However, fundamental understanding of the properties of oxygen vacancies in metal oxides is far from complete, results are scattered across the literature and an unified view of their properties is still lacking [10]. In this review, we attempt to systematize these data, including also the first principles results obtained during recent years for new prospective materials and composites. At least three following reasons for the steadily growing interest in oxygen vacancies, both experimental and theoretical, could be mentioned:

i. various metal oxides attract renewed interest because of their relevance to promising technological applications achieved because of their nonstoichiometry; in particular, the presence of *F* centers is crucial for the performance of solid oxide fuel cells, sensors, and microelectronic devices, as well as in degradation control of damaged insulators [10];

ii. outstanding achievements in the microscopic identification of individual oxygen vacancies on the metal oxide surfaces, i.e., (a) on $TiO_2(110)$ by atomic force microscopy (AFM) combined with AFM simulations [11] and (b) on $SrTiO_3(001)$ by scanning transmission electron microscopy (STEM) combined with reflection high-energy electron diffraction (RHEED) and atomic-scale electron energy-loss spectroscopy (EELS)[12];

iii. rapid improvement of computer hardware and generation of efficient computer codes for ab initio calculations on variety of model materials have enabled theorists to treat objects of increasing complexity [9], including point defects in metal oxides (bulk and surface).

The recent achievements in the theory of point defects in bulk and on crystalline surfaces are connected with the widespread application of cluster and periodic models and computer codes developed for molecular calculations or for perfect crystals, including metal oxides, respectively [6–9]. This allows us to study changes induced by a point defect in the bulk or on the surface: additional local energy levels in the optical gap, local lattice relaxation around defects, influence of the point defects on the surface stability, adsorption energy of atoms, and molecules on defective substrate, etc. Detailed analysis of theoretical aspects of defect simulations in metal oxides is presented in Section 2 (Theoretical Background). It has long been realized that neither periodic nor cluster models could alone give an accurate picture of defect properties [7]. From the beginning, a significant challenge of periodic models was their disability to describe charged and excited states of defects as well as their agglomerates; however, these problems, at least at the theoretical level, were formally solved [13–15]. At the same time, despite the fast methodological development of cluster models (both embedded and molecular [7]) for simulation of defects in solids [16, 17], they still face a serious challenge in the proper description of oxygen vacancies in metal oxides with chemical bonding of a partly covalent nature, especially in ternary (ABO_3) and more complicated oxides (both bulk and surface). Thus, for a consistent description of oxygen vacancies in a broad family of metal oxides, we choose here models with periodic boundary conditions [9].

In this review, we consider mainly isolated neutral *F* centers in metal oxides (oxygen vacancies with the two trapped electrons). Except for some examples, important from the methodological point of view, we do not consider other kinds of defects, for example, metal vacancies (cation centers), oxygen and metal interstitials, substituents, impurities (hydrogen, nitrogen, carbon, etc.), charged and excited *F* centers, as well as hole centers (see [1–9]). We also do not analyze the interaction of defective oxide substrates with adsorbed gas atoms and molecules (oxygen, nitrogen, water, etc.). We mostly focus on the limit of well-separated, single oxygen vacancies, which practically do not interact with

each other [18]. However, in some oxide systems the concentration of oxygen vacancies could be high enough to produce qualitative changes in the crystal properties; the same is true also for the interface between a defective oxide substrate and a transition metal overlayer [19].

In particular, we analyze the structural and electronic properties of F centers in bulk, surface, and interface with transition metals for binary oxides of light metals, MgO and Al_2O_3 (Section 3) and ternary metal oxides $SrTiO_3$, $BaTiO_3$, $PbTiO_3$, $KNbO_3$, and $PbZrO_3$ (Section 4). We analyze and compare: (i) the structural relaxation around a point defect and relaxation energy; (ii) the vacancy formation energy; (iii) the energy barrier for vacancy diffusion; (iv) the electronic charge redistribution around a vacancy; (v) the band structures and densities of states for defective bulk and surface. A considerable fraction of the results analyzed in Sections 3 and 4, is obtained in our own studies. Special attention is paid to the relation between the F center properties and the chemical nature of the host crystal.

2. Theoretical Background: Defective Crystal Models and Calculation Schemes

The calculation schemes usually used for first principles point defect modeling include: (i) the choice of a *model* of the defective crystal: periodic or cluster; (ii) the choice of the *Hamiltonian:* Hartree–Fock (HF), Density Functional Theory (DFT), or hybrid DFT + HF; (iii) the choice of the *basis set* for the one-electron function decomposition - crystalline orbitals as Linear Combination of Atomic Orbitals (LCAO) or Plane Waves (PW).

2.1. POINT DEFECT MODELS IN A BULK CRYSTAL

Three general models are used in the defective crystal calculations: (i) a local non-periodic cluster (embedded, molecular or free), (ii) a cyclic cluster, and (iii) a supercell [20].

All these models assume that the electronic states of a single defect in a crystal are well localized within a relatively small spatial region around the defect. The degree of this localization depends on the nature of the point defect and of the host crystal. In the wide-gap metal oxides (like ionic

MgO or partly covalent $SrTiO_3$ crystals) the defect energy levels are separated sufficiently far from the perfect crystal bands (>0.3 eV). Thus, the corresponding defect electronic states are localized in a relatively small crystal volume. In this case the obvious approach to modeling is to separate the *defect region* where the crystal is perturbed from the perfect crystalline background, and to treat only the former in an explicit manner.

In *the cluster model* at least one sphere of atoms has to be included between the defect region and the cluster surface, which remains unperturbed. However, the explicitly treated part of the crystal should, in principle, extend far enough so that the defect influence is negligible [21], up to the point where the amplitude of the defect-localized wave functions and charge density redistribution become negligible. The cluster chosen in such a way is then handled explicitly at any given level of calculation used for molecular systems.

The main problem for cluster models arises in representing the rest of the crystal; there are different possibilities for this representation. In cluster models: (i) a group of atoms chosen is incorporated into the crystalline environment (embedded cluster), (ii) surface atoms are saturated by hydrogen or other atoms (saturated molecular cluster), (iii) in the simplest case, the free cluster (neutral or charged) is used where the rest of the crystal is neglected. The most refined embedding methods are based on the quantum treatment of the rest of the crystal based upon Green's functions [22, 23]. However, such an embedding approach is computationally demanding and faces convergence problems in the self-consistent procedure.

The two models with Periodic Boundary Conditions (*supercell* and *cyclic cluster*) allow us to calculate the one-electron states of perfect and defective crystals at the same level of approximation. This point becomes important when one is interested in position of the defect levels in the band gap of a perfect solid.

The supercell model (SCM) and cyclic cluster model (CCM) have both similarities and significant differences [24]. Similarity exists in that, in both models, not a standard primitive unit cell but an *extended* unit cell (supercell or large unit cell) is considered. The discrepancy is that the periodic boundary conditions in the SCM are introduced in **k**-space for the infinite crystal or its main region, but in the CCM model–for the extended unit cell itself. The cyclic cluster model is conceptually a supercell-like approach but is technically more

closely related to the simple molecular cluster model. The SCM introduces the artificial point defect periodicity, whereas the CCM describes the single point defect.

In the SCM, the calculations with HF or hybrid Hamiltonians are performed so far in LCAO basis expansions, while DFT Hamiltonians are used both in the LCAO and PW representations. CCM can be practically realized only with semi-empirical LCAO Hamiltonians [24]. It should be mentioned that semi-empirical LCAO methods, being simplified HF approaches, permit large-scale CCM modeling of the atomic and electronic structure of materials using, for example, Intermediate Neglect of Differential Overlap (INDO) [25] and Modified INDO with Symmetrically-orthogonalized orbitals (MSINDO) [24, 26]. They were used successfully for modeling of many properties of point defects. Some results obtained using these approaches for CCM simulations are presented in Sections 3 and 4, in comparison with data obtained using ab initio calculations in the SCM models.

In SCM the defects are distributed periodically. As the extended unit cell becomes larger, the defects are separated by defect-period large distances and do not affect each other, then results of SCM and CCM models application should converge. The *band width* of defect states depends primarily on the overlap of the functions describing the defect electronic states in neighboring supercells and decreases rapidly with increasing the *defect period*. Therefore, this bandwidth can be used as a criterion of the convergence of the SCM results to those of CCM and to an isolated defect model.

In most of theoretical approaches to defective crystals their symmetry is taken into account [27]. A single defect embedded into a crystal disrupts the translational symmetry of a perfect crystal so that it may be considered as a huge molecule with a point symmetry group inherent to molecules. There are two cases: an *atomic-type* point defect which occupies a single lattice site or an interstitial position (e.g. a substitutional impurity, vacancy, or interstitial atom) and a *molecular-type* point defect, which occupies several sites and can be composed of an impurity molecule or a cluster of several neighboring vacancies. In the first case the symmetry group of the defective crystal is fully determined by the *site symmetry* of the position **q** of the defect. In a crystal with a symmorphic space group the defect may occupy the position **q** with the symmetry of the crystal class or one of its subgroups. In nonsymmorphic crystals the point group of the crystal

with a single defect is always a subgroup of the crystal class. In a crystal with point defects of a molecular type the impurity molecule is centered at a point with some site symmetry. A molecular defect has its own point symmetry so that the point symmetry of the whole system is determined by the common elements of two groups: the point group of the isolated molecule and the site symmetry group of the site centered on the impurity molecule.

It might be assumed that when a point defect appears, the crystalline matrix around the defect does not relax (the *rigid lattice* model). In reality this assumption is approximately correct only for a few point defects and, as a rule, only for the ground electronic state. In most modern first principles calculations local lattice structure is calculated self-consistently. The distribution of the defect electrons significantly disturbs the atoms surrounding the defect so that the point symmetry of the entire system may change. The knowledge of the actual symmetry of a crystal with a point defect is necessary for understanding its properties: the symmetry determines the selection rules for optical transitions in the defect, the symmetry and the splitting of local energy levels in external fields, the features of EXAFS, EPR, ENDOR, and NMR spectra, etc.

To understand the nature of a point defect in a crystal and how it affects properties of the crystalline matrix, it is necessary to combine the local energy levels of the defect and the band structure of the perfect crystal. However, these two systems (crystal with a defect and perfect crystal) have in general different symmetry and the classification of electronic states is made according to irreducible representation (*irreps*) of either a point group (for a crystal with a single defect) or a space group (for a perfect crystal).

In the molecular cluster model, it is rather easy to establish the relationship between energy levels and one-electron states of a molecular cluster with and without a point defect. The symmetry of both systems is described either by the same point group or by a subgroup of another group (in the case of a molecular-type defect). Hence, in the cluster model the relationship is simple between the classification schemes of electron energy levels and states of perfect and imperfect crystals, whereas the relationship between the cluster electron energy structure and that of a perfect crystal is much more complicated.

In models using the Born–von Karman periodic boundary conditions it is convenient to use the site symmetry approach [27]. The single-defect local-

ized electron states of a given energy level span the space of an irreducible representation of the defect point symmetry group $G\{q\}$. The band states of a perfect crystal are classified according to *irreps* of the space group G. It is useful to determine which band and localized states are allowed by symmetry to mix (e.g., for calculating the electronic structure using LCAO basis functions).

The supercell is defined by a linear tranformation connecting the basis translation vectors of the perfect crystal a_i with the translation vectors A_j of the supercell chosen:

$$A_j = \sum_{i=1}^{3} l_{ji} a_i \quad |\det 1| = L \qquad (1)$$

The translation vectors A_j and their integer linear combinations

$$A_n = \sum_{j=1}^{3} n_j A_j \qquad (2)$$

define the new Bravais lattice. The volume of the supercell is L times larger that that of the primitive cell. The point symmetry of the new Bravais lattice is defined by the choice of the matrix in Eq. (1). When the point symmetry of the initial and transformed lattices coincides (the type of the lattice may be also different), the transformation (1) is called a *symmetrical* supercell transformation. For $L = 1$ transformation (1) means transition to other basic translation vectors (another shape but with the same volume). The well-known crystallographic unit cells for face-centered and body-centered lattices are examples of symmetrical supercell transformation for $L = 4$ and 2, respectively. A number of examples for different lattice structures are presented in Refs. [18, 20, 21, 28] while examples of the transformation matrices are presented in Section 4.1.1 for vacancy-containing ternary metal oxides with simple cubic structure.

The crystal supercell with a point defect serves in fact as the primitive unit cell of the new periodic structure. The latter could be calculated using any standard method for perfect solids as the symmetry of the "new" crystal is described by one of the 230 space groups. Therefore, the one-electron states in both the perfect and defective crystals are defined by the Bloch functions which may be represented in terms of the LCAO or PW basis sets. The Brillouin

zone (BZ) of the defective crystal is obtained by folding of the BZ of the perfect crystal which is defined by the transformation, Eq. (1). In any case, the defective crystal BZ is L-times smaller than that of the perfect crystal. The perfect crystal calculation in the supercell model simply means the *reclassification* of the one-electron states [27]. The defective crystal calculation in the supercell model allows us to estimate the supercell shape and size corresponding to the single point defect. Such a study requires the calculation of defective crystals for a series of supercells of increasing size. As the point defect period also increases, the energy sub-band formed by the local states becomes more and more flat leading in the limit the single point defect *energy level* in the band gap.

2.2. POINT DEFECT MODELS EFECTS ON CRYSTALLINE SURFACES

The study of point defects on crystalline surfaces requires the definition of the pure surface model and subsequent supercell calculations of the defective surface (the surface with a single point defect). To model the crystalline pure surface, the following basic approaches are used: the molecular cluster (non-periodic) model and two periodic models—*a single slab* (with two-dimensional periodicity) and *a repeated slab* (with three dimensional periodicity).

In the molecular cluster approach a crystal with a surface is modeled by a finite system consisting of the atoms on the surface and several neighboring atomic planes. The symmetry of such a model is described by one of the standard 32 crystallographic point groups. Thus, the calculation schemes of molecular quantum chemistry can be directly applied to the molecular cluster model of the surface. In many cases, influence of the surrounding crystal on the surface is modeled by either the field of atomic cores (in the pseudopotential approximation) or just by point charges (the Madelung field).

In the *single slab* model, a crystal with a surface is treated as a two-dimensional (2D) slab of finite thickness. Its symmetry group contains the symmetry operations obtained by moving the atoms out of the plane of the layer but bringing them into positions occupied by other atoms of the slab. These are space *diperiodic groups* in three dimensions, called the *layer groups.* 80 diperiodic (layer) groups DG are the symmetry groups of three-dimensional (3D) objects with 2D periodicity and belong to so-called *subperiodic groups* [20]. DG contains a subgroup $T^{(2)}$ consisting of two-dimensional translations:

$$\mathbf{a}_n = n_1\mathbf{a}_1 + n_2\mathbf{a}_2, \qquad (3)$$

where vectors $\mathbf{a}_1$ and $\mathbf{a}_2$ describe the two-dimensional plane lattice.

The relationship is known between space and subperiodic groups: given a crystal of a specific space group symmetry and a plane transecting the crystal, one can enquire as to what is the layer subgroup of the space group which leaves this plane invariant. This problem arises, for example, in surface modeling by a single slab. The surface atom relaxation may reduce the point symmetry of the slab model compared to that discussed for the unrelaxed surface.

In PW first principles calculations only the *periodic (repeated) slab* model is used. In this model the slab is periodically repeated along the *z*-axis normal to the slab surface plane restoring the 3D periodicity of the model. The symmetry group of the periodic slab is one of 230 three-dimensional space groups.

In the single slab model, the two-dimensional periodicity (and the corresponding 2D BZ-2) is described by one of five plane lattices. This lattice is defined by the surface chosen. The surface is identified by three integers (*hkl*) - *Miller indices*, specifying atomic planes in the crystal by means of the components of a vector perpendicular to that plane.

Planes, perpendicular to crystallographic axes *X*, *Y*, and *Z* are indicated as (*h*00), (0*k*0), and (00*l*), respectively. In particular, the planes closest to the origin are identified with indices (100), (010), and (001). Planes parallel to one of the three axes *X*, *Y*, and *Z* are indicated (0*kl*), (*h*0*l*), and (*hk*0), respectively. When the surface reconstruction effects (change of the surface plane translational symmetry with respect to that in a perfect crystal) may be neglected, the symmetry group of a crystal with a surface is a subgroup of the bulk crystal group. However, the BZ-2 depends on the indices of surface plane. For example, in the crystals with face-centered cubic Bravais lattices the plane lattices are square, rectangular and hexagonal, for the (001), (110), and (111) surfaces, respectively. In particular, the single slab of (001) surfaces of MgO and SrTiO$_3$ crystals possess 2D periodicity of the square plane lattice. The number of atoms in the two-periodic unit cell depends on the slab thickness (number of atomic planes parallel to the surface). For an ionic MgO-like crystal, 3–5 atomic planes are sufficient to determine surface properties, whereas for partly covalent compounds (like SrTiO$_3$) it is necessary to consider thicker slabs with 7–11 atomic planes. In any case, the dependence of the results (surface energy, charge distribution) on the slab thickness has to be studied first of all for the pure surface.

When using the repeating 3D periodic slab model, one needs also to study the dependence of the results on the so-called vacuum gap (the inter-slab distance). As it was shown for the MgO crystal, increasing the vacuum gap for a fixed slab thickness moves the results to those corresponding to a single slab of the same thickness [29].

In the single slab approach, a single point defect on the surface is modeled by the 2D supercell defined by the transformation Eq. (1) for *j* = 1,2 and the planar lattice basic translation vectors $\mathbf{a}_1$ and $\mathbf{a}_2$ as defined in Eq. (3). As in the 3D case, the symmetrical transformation maintains the point symmetry of the planar lattice (C_i, C_{2v}, C_{4v}, and C_{6v} for the oblique, rectangular, square, and hexagonal plane lattices, respectively). For fixed slab thickness (and vacuum gap in the repeating slab model), the convergence of the surface point defect calculations should be studied with respect to the increase in size of the 2D supercell.

2.3. HAMILTONIANS FOR POINT DEFECT CALCULATIONS

The Hamiltonians used in supercell modeling of point defects in the bulk crystal and on the surface are the same as those used in calculations on the perfect bulk solids. The one-electron Bloch functions depend on the wave vector $\mathbf{k}$, belonging to the 3D BZ for the point defects in the bulk and in the repeating slab model or to the BZ-2 in the single slab model. There exist HF, DFT approaches as well as the hybrid HF-DFT Hamiltonians. In the DFT approach, the Kohn–Sham (KS) one-particle equations are solved. Single particle orbitals are combined with Fermi-Dirac occupation numbers to construct self-consistency of electron densities. In calculations on magnetic systems, e.g., certain perovskites, oxides of *d*- and *f*-metals, *spin-polarized* calculations are performed, where orbitals of spin up and down are treated separately.

The HF and KS crystalline orbitals are expanded onto a *basis set* (LCAO or PW). For the periodic system the basis set symmetrization over the translation subgroup of the space group is used, leading to the Bloch sums of AO over the translation vectors of the direct lattice or PW over the reciprocal lattice.

The Hamiltonian $F(\mathbf{k})$ consists of one-electron $H(\mathbf{k})$ and two-electron $G(\mathbf{k})$ parts. The $G(\mathbf{k})$ differs in HF and DFT methods: in the former case it

consists of Coulomb and exchange parts, in the latter case exchange is replaced by the so-called exchange-correlation functional. The Hamiltonian matrix elements contain the sums over translation vectors of the direct lattice (LCAO basis) or reciprocal lattice (PW basis). In both cases the summation of occupied states over BZ is necessary to perform the self-consistent density matrix calculations. The traditional Monkhorst–Pack [30] special **k**-point sets are widely used for the BZ summation. The incorporation of the exchange and correlation interactions within KS DFT is non-trivial since the exact functionals are not known except for the homogeneous (uniform) electron gas, leading to unavoidable approximations in the calculation of real systems.

The simplest DFT approximation is the local-density approximation (LDA), based upon the exact exchange energy for a uniform electron gas, which can be obtained from the Thomas–Fermi model, and from fits to the correlation energy for a uniform electron gas. In different semilocal, generalized gradient approaches (GGA) the energy dependence on the electron density gradient is taken into account. Nowadays, the most popular (and most reliable) GGA functionals are PBE (the functional proposed in 1996 by Perdew et al. [31]), and BLYP (denoting the combination of Becke's 1988 exchange functional [32] with the correlation functional of Lee et al. [33]). Another widely used functional PWGGA denotes the GGA functional, suggested by Perdew and Wang [34]. Many other GGA-type functionals are also available, and new ones continue to appear. The known functionals are also occasionally modified, as it has been done for the PBE functional, to improve its accuracy for thermodynamic and electronic properties of molecules [35].

To improve the LDA and GGA models, orbital-dependent functionals are introduced. The introduction of orbital dependence (not only density and gradient dependence) into the functionals can be realized in different ways: self-interaction correction (SIC), screened exchange, inclusion of the kinetic energy dependence on the density functional, etc. [20] *Hybrid* HF-DFT functionals are the most popular beyond-GGA functionals which mix a fraction of HF exchange into the DFT exchange functional and use the DFT correlation part.

Three-parameter functionals known as hybrid B3PW and B3LYP were developed:

$$E_{xc}^{B3PW} = E_{xc}^{LSDA} + a(E_x^{HF} - E_x^{LSDA}) + b\Delta E_x^{Becke} + c\Delta E_x^{PW}$$

$$E_{xc}^{B3LYP} = E_{xc}^{LSDA} + a(E_x^{HF} - E_x^{LSDA}) + b\Delta E_x^{Becke} + c\Delta E_x^{LYP},$$

$$(4)$$

where xc means exchange-correlation and x means non-local exchange energy.

The B3PW functional uses the Becke [32] exchange and Perdew–Wang exchange-correlation [36], while in the B3LYP functional - the correlation part is that suggested by Lee et al. [33]. The a, b, and c parameters were fitted to an extensive set of experimental data. These hybrid functionals were implemented in different upgrades of the *CRYSTAL* code using localized LCAO representation of crystalline orbitals [37]. This solves a key problem of DFT calculations on insulators and semiconductors - underestimate of the band gaps thus lifting shallow defect states, which should lie below the conduction band (CB) bottom, into the CB [18]. To solve the same problem for PW Hamiltonians, the first solution was found to be implementation of the DFT+U method (U is the spherically averaged Hubbard parameter characterizing the Coulomb repulsion energy cost to place an extra electron on a particular site [38]), as recently implemented in the *VASP* code for both LDA and GGA approximations [39]. However, a more reliable solution of the underestimated band gap in PW calculations could be implementation of hybrid HF-DFT functionals in the computational procedure [40], expected soon in VASP.

In solid-state calculations, the use of hybrid functionals has a high computational cost for the exact HF exchange. A recent alternative to the conventional hybrid functionals is found to be a screened exchange hybrid functional developed by Heyd, Scuseria, and Ernzerhof (HSE) [41]. A screened Coulomb potential is used in this functional for the exact exchange interaction, drastically reducing its computational cost, and providing results of similar quality to traditional hybrid functionals. It was demonstrated that the screened HF exchange (neglect of the computationally demanding long-range part of HF exchange) exhibits all physically relevant properties of the full HF exchange. The application of different hybrid functionals in solids properties calculations was demonstrated in a review article [42].
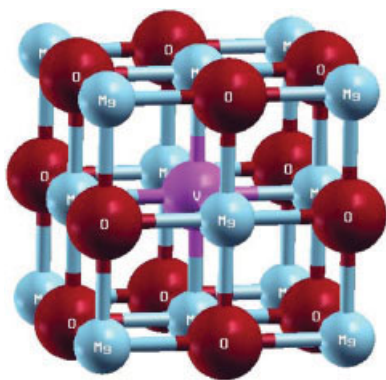
FIGURE 1. The local environment of the oxygen vacancy (*V*) in bulk MgO. Six Mg nearest ions, 12 next-nearest O ions and 8 more remote Mg ions are shown. [Color figure can be viewed in the online issue, which is available at www.interscience.wiley.com.]

3. Defects in Binary Oxides of Light Metals

3.1. MAGNESIA

The *F* centers are well known in cubic alkali halides and alkali earth oxides including MgO. In the only stable face centered cubic (*fcc*) structure of magnesia crystal described by $Fm\bar{3}m$ (O_h^5) space group with a lattice parameter 4.21 Å [2], the oxygen vacancy is surrounded by the six nearest equivalent Mg ions and 12 next-nearest O ions (Fig. 1). The *F* centers in MgO do not reduce the local symmetry around each of them (O_h) since the vacancy is positioned at the center of co-ordinates (0,0,0). The abundance of reliable experimental data and structural simplicity [2] as well as wide physical and chemical applications of magnesia [3, 7] facilitated extensive theoretical studies on *F* centers in both MgO bulk and surface. Practically every computational technique was tested on oxygen vacancies in magnesia: (i) periodic DFT and HF calculations [4, 10, 43–45]; (ii) the DFT and HF calculations on embedded [46–49] and molecular [6, 50, 51] clusters, respectively; (iii) semi-empirical embedded [3, 52] and molecular [53] cluster calculations by means of the INDO and MSINDO methods, respectively. According to most of these studies, an electronic charge close to 2 *e* is localized inside the vacancy in the ground state of a neutral *F* center. This electronic charge is well trapped in the vacancy because of the electrostatic stabilization due to the large Madelung potential of the ionic crystal [50]. However, this is no longer the case for the excited state of the *F* center.

3.1.1. Bulk

The *F* center in MgO bulk in the ground state produces an *s*-type deep level in the band gap accompanied by a small and fully symmetric (O_h point group) relaxation of the surrounding ions. For the neutral O vacancy, most of calculations predict a minimal outward displacement of neighboring Mg cations, ranging from 0.25% in VASP calculations [10] up to 2% in semi-empirical INDO calculations [3]. The next coordination sphere consisting of oxygen anions was found to be slightly compressed [3, 46]. Correspondingly, different ab initio calculations resulted in very moderate values of the lattice relaxation energy (up to 0.02 eV in periodic LDA PW [43] and 0.05 eV in embedded cluster HF calculations [46]).

Recent VASP calculations of the *F* center using a 3×3×3 MgO supercell (i.e., ~3% of defect concentration with the nearest interdefect distance $d_{F\text{-}F} \approx$ 12 Å) [10] have shown that the repulsion between the nearest vacancies does not exceed 0.02 eV, which is usually considered as a good approximation of a single point defect [18]. As to the formation energy of a single oxygen vacancy, it was found here to be ~ 10 eV [10], which agrees to within 20% with earlier estimates (cf. 8.7 eV obtained using embedded cluster HF [46] and 10.5 eV in periodic LDA PW calculations [43]). The oxygen vacancy formation energy in magnesia bulk was experimentally determined in additively colored samples to be 1.53 eV larger than the experimentally measured cohesive energy, 10.35 eV, i.e., 11.88 eV [54].

The saddle point of the vacancy *diffusion* path in MgO bulk is located halfway between the two O sites along the (110) axis. The activation barrier for this diffusion was found to be overestimated in recent VASP calculations [10] (4.2 eV vs. 3–3.4 eV in experiment on additively colored crystals [3, 55]). Surprisingly, the INDO calculations [3] gave the diffusion energy much closer to experiment than the first principles VASP calculations for magnesia bulk. However, recent results of VASP calculations on an F_s center at the MgO (001) surface [44] provide a possible reason for this difference, as explained in next Session 3.1.2.

As mentioned in Section 2, most previous ab initio and semi-empirical calculations could not reproduce the band gap properly; the experimental value of 7.84 eV [56] is overestimated in HF calculations by about a factor of two whereas DFT PW calculations greatly underestimate this value (4.8 eV [43]). Nevertheless, the position of the defect

level above the valence band edge turns out quite reasonable, ~2.7 eV in both periodic DFT PW and embedded cluster HF calculations [43, 46]. The first optically excited state is known to be close to the conduction band bottom. However, the periodic first principles calculations, unlike the embedded cluster HF approach [46], are not suited well for excited state calculations and cannot estimate optical absorption energy properly. As to semi-empirical calculations [3, 52], a good agreement with experiment (4.8 eV) is achieved since parameters of the method are fitted to reproduce the property.

3.1.2. The (001) Surface

According to Tasker's classification for ionic crystalline compounds [57], the (001) surface with rock-salt structure is the most energetically stable among densely packed faces of the same *fcc* single crystal. However, even the most stable MgO (001) surface can be reconstructed under real experimental conditions: surfaces of cleaved, polished, powdered and other types of magnesia samples are usually known to be very rough on the atomic scale and contain many steps and other low-coordinated sites, such as kinks and corners [58]. As to polar surfaces of MgO like (111), they are expected to cause near-surface charge redistribution and reconstruction, which is difficult to sort out experimentally [59]. Atomistic simulations provide insights about the energetics of surface reconstruction, and give indications on mechanisms of energy reduction for polar surfaces, which could hardly be obtained by direct electronic structure approaches. For example, it was shown [60] that the MgO (110) surface should reconstruct to a zigzag microfaceted (001) structure, with a surface energy reduced by 50%. (Our comparative ab initio simulations on both (001) and (110) MgO substrates [61] confirmed the energetic preference of the former.) Similarly, the polar MgO (111) surface also reconstructs by faceting into non-polar (001) surfaces [60].

In comprehensive DFT PW simulations on the defective MgO (001) surface using both periodic models [43, 45] and embedded clusters [47] both flat and reconstructed magnesia substrates were considered. Despite use of different models in these studies, the results are quite similar. It was found that for the surface F_s center, the neighboring Mg ions relax away from the vacancy on the surface x–y plane, with displacements larger than in the bulk (cf. 0.5 and 0.25%, respectively) [43]. In addition, the surface Mg neighbors of an oxygen vacancy reveal

a 1% displacement component along the z-axis perpendicular to the surface. The magnesium ion directly below the surface oxygen vacancy relaxes away from the F_s center even more, by 1.25%. Similar relaxations of nearest Mg ions on-plane and neighbors along the z-axis (1–1.5%) were obtained also in the embedded cluster DFT PW calculations [47–49]. In molecular cluster HF calculations [50a], the averaged value of outward Mg ion relaxation was found to be larger (1.8%). Some discrepancy was found for the next-neighboring oxygen atoms: embedded cluster DFT PW calculations give outward relaxation (0.25 [49] and 0.75 [48] %) vs. inward relaxation in molecular cluster HF (-1.3% [50a]). On the reconstructed MgO (001) surface, relaxation of the atoms nearest to the F_s center is not so trivial due to overlap of the local defect relaxation and of defectless surface relaxation. The most reliable estimate is from the calculations [42], suggesting the relaxation energy of 0.06 eV for the flat (001) surface, 0.07 eV for the step, 1.04 eV for the corner, and 0.16 eV for the reverse corner (cf. 0.02 eV in bulk [42]). Inside the reverse corner the F_s center is fivefold coordinated analogously to a flat surface, while at a step this coordination is reduced to four, and on the corner to three.

Our periodic HF calculations on the defective MgO (001) substrate [44] show that for a 3×3 surface supercell with the F_s center the defect level dispersion (0.15 eV) is still too high to consider this defect as isolated, thus contrasting with much smaller dispersion (0.02 eV) obtained in VASP calculations for a bulk F center per 3×3×3 MgO supercell [10]. Although different computational schemes were used in both calculations, this difference demonstrates a larger delocalization of defect states on the surface. The Mulliken population analysis [44] shows the charge of 1.72 e inside the vacancy and 0.28 e distributed over the two nearest Mg and O spheres of ions. In embedded cluster DFT calculations, the electronic charge of F_s center was found to be smaller, ~1.5 e [47]. Our later periodic DFT-LCAO calculations [62] confirmed that magnitude of the charge (1.55 e), i.e., difference between the methods (HF vs. DFT) more strongly affects the results than any difference in the two models (supercell vs. cluster). Qualitatively, molecular cluster HF calculations [50] confirm that a certain fraction of the electronic density is delocalized over the Mg ions.

Periodic LDA PW calculations predict the formation energy of the F center on the flat MgO (001) surface to be 9.55 eV [43] (cf. 9.4 eV obtained

in the periodic VASP calculations [45], as well as 9.1, 7.7, and 12.1 eV using an embedded [47] and two molecular [50a, 53] cluster models, respectively). Thus, the surface formation energy is ∼1 eV smaller than in bulk magnesia. This could be explained by a different coordination of the *F* center surrounding (five nearest Mg ions on the surface instead of six in the bulk). Moreover, the O vacancy formation energy on a flat magnesia surface [45] is not largely affected by thickness of the slab when varied from 2 to 12 layers, i.e., thin MgO (001) slabs (at least three layers) are quite suitable models for the proper description of surface properties. The formation energies for the F_s center at the step, the corner and the reverse corner were also found to be smaller than in the bulk, i.e., 9.0, 8.1, and 9.4 eV, respectively [43].

A complete description of a defective oxide surface requires also the calculation of the activation energies for defect diffusion along and across the surface [45]. For a MgO (001) surface modeled by a 12-layer slab, the surface diffusion through terrace sites has the activation energy of 2.69 eV, whereas diffusion from the surface to the subsequent layers has larger energy barriers: 3.42 eV - from the surface to the subsurface layer, 3.93 eV - from the subsurface layer to a deeper layer, 4.13 eV - for the next interlayer diffusion, thus converging to the value of 4.21 eV for bulk diffusion [10]. The difference between the energy barriers described here is large enough to conclude that whenever oxygen vacancies exist at the surface, surface-parallel transport occurs already at lower temperatures and always prevails while oxygen vacancies in deeper layers of the material tend to be more static [45].

The surface top valence band (VB) was found to lie 6.7 eV below the vacuum level in embedded cluster DFT PW calculations [47], in good agreement with the MIES data [63] predicting 6.7±0.4 eV. Meanwhile, the band gap of the defected MgO (001) surface is narrowed by ∼1.6 eV as compared with that in MgO bulk, due to the formation of surface states at the bottom of conduction band (CB) [43]. The level of the F_s center at the top surface layer, according to the same embedded cluster calculations [47], lies about 3 eV above the top of the surface VB, which is in a fair agreement with the result of periodic LDA PW calculations predicting 2.3 eV for the defect on a flat MgO (001) surface [43].

3.1.3. Interfaces with Metal Films

Technologically important interfaces between the simple metal oxides (e.g., MgO) and transition metals continue to attract great attention due to numerous applications in microelectronics and nanoelectronics, optical devices, catalysis, and giant magnetoresistance [64–67]. In spite of numerous first principles simulations on (i) transition metal adlayers with varying density of regularly distributed adatoms on magnesia substrate [61, 68–74] and (ii) single metal atom or several-atom clusters over embedded or molecular cluster of the same substrate [50b, 75–80], theoretical understanding of the adsorption nature for Ag, Au, Cu, Fe, Ir, Nb, Ni, Pd, Pt, Rh, and Ru atoms on the oxide substrate remains a challenging problem since quite different computational methods and models led to a variety of results, even for a simple non-polar MgO (001) substrate. Not surprisingly, practically all ab initio calculations give the energetic preference for the positions of the metal adatoms over the surface oxygen ions on the MgO (001) substrate; however, significant details differ from method to method.

For single metal atom adsorption, both periodic and cluster models could be used with the corresponding choice of large surface supercells and clusters. At the same time, most periodic calculations on metal monolayer (1 ML) and moderate ≥0.5 ML coverages of substrate did not take into account the interfacial lattice misfits. In the semi-coherent case (several per cent of misfit), a two-dimensional network of misfit dislocations is introduced to accommodate the misfit strain, and interface areas between misfit dislocations can be also regarded as coherent structures. For example, the coherent-model simulation on the Ag/MgO (100) interface (semi-coherent in reality) performed in Ref. [68] then was corrected for the energy of misfit dislocations. For the semi-coherent oxygen-terminated Cu/MgO {222} interface [81], it was found quite possible to represent its properties as average of the interface properties for different symmetric coherent structures. However, when a lattice misfit of the metal/oxide interface exceeds 10%, the interface structure cannot be described by arrays of misfit dislocations, as found for semi-coherent interfaces [82].

Along with ab initio calculations on the metal/magnesia interfaces, several other atomistic semi-empirical approaches were developed as well, e.g., the image interaction model (IIM) [83] and the shell model (SM) [84]. In contrast to widespread ab initio
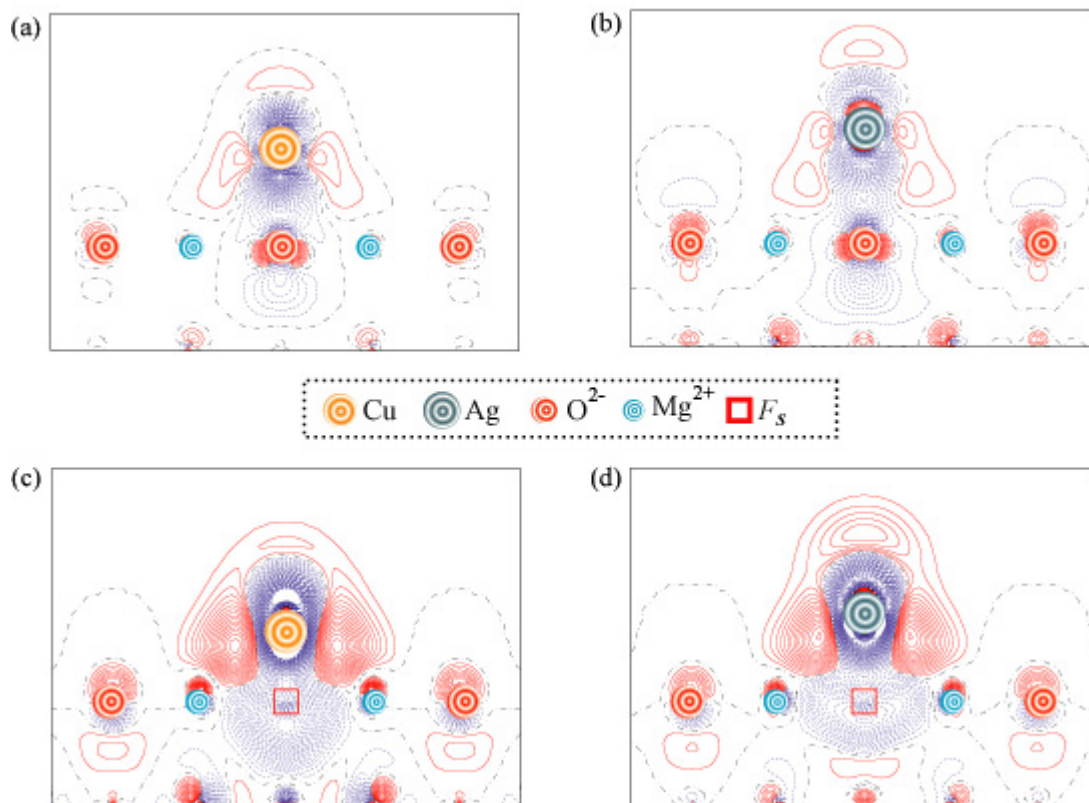
FIGURE 2. 2D difference electron density plots (the total density in the perfect Me/MgO(001) interface minus the sum of electron densities of both isolated metal overlayer and MgO substrate) projected onto the (100) section plane (Fig. 1) for 0.25 Me ML coverage: (a) Cu and (b) Ag over regular (001) surface as well as (c) Cu and (d) Ag atop F_s center regularly distributed with the same 0.25 ML periodicity [19, 62]. Dash-dot (black) isolines correspond to the zero level. Solid (red) and dash (blue) isolines describe positive and negative values of electron density, respectively. Isodensity increment is 0.002 e Å^{-3}. [Color figure can be viewed in the online issue, which is available at www.interscience.wiley.com.]

simulations on adlayers or clusters of numerous transition metals of varying atomic density over the defect-free MgO (001) substrate, the number of theoretical studies, which consider the *morphology* of metallic film growth on oxide substrate, including formation of 3D islands, is still very limited. Our recent studies on Ag and Cu adhesion over defect-free MgO (001) surface [73, 85, 86], which combine periodic DFT-LCAO calculations on the regular interfaces with statistical thermodynamic treatment based on model mixing potentials, give successful prediction of metallic film growth mode. Recently, we theoretically predicted that 3D metallic clusters growing on the MgO (001) substrate possess pyramid-like shape [86] which was indeed experimentally observed [66]. Even for relatively low concen-

tration of the metal vapor, the 3D clusters may grow up to several-plane height.

In spite of significant experimental and theoretical efforts undertaken to clarify influence of the surface point defects (mainly F_s centers) [19, 44, 45, 48–50, 62, 63, 83, 84, 87–92] on the interfacial properties, it is still unclear how defects affect the nucleation and growth of different metal overlayers. By controlling the nature and density of point defects on oxide surfaces, one envisions a novel means of tailoring wetting, adhesion, and dispersion of metal particles and films [19]. The kinetic approach [93, 94] considers the surface point defects as nucleation sites for metallic islands growth. However, ab initio calculations [87b] have shown that the propensity for neutral anion vacancies to

TABLE I

Comparison of the adsorption properties for regular and defective interfaces obtained in our studies [19, 62, 74] and in Ref. [48].

Adatom over surface site	Metal adatom	Adsorbate coverage	Distance to substrate $z_{Me}^{(o)}$, (Å)	Adsorption energy per adatom (eV)	Charge transfer $\Delta q_{Me}{}^a$, e
O^{2-} ion	Ag	0.25 ML	2.50 Ref. [62]	0.40 Ref. [62]	0.031 Ref. [62]
			2.55 Ref. [48]	0.41 Ref. [48]	—
		1 ML	2.97 Ref. [74]	0.17 Ref. [74]	0.007 Ref. [74]
	Cu	0.25 ML	2.08 Ref. [62]	0.62 Ref. [62]	0.047 Ref. [62]
			2.03 Ref. [48]	0.80 Ref. [48]	—
		1 ML	2.36 Ref. [74]	0.33 Ref. [74]	−0.007 Ref. [74]
Mg^{2+} ion	Ag	0.25 ML	2.83 Ref. [62]	0.38 Ref. [62]	0.009 Ref. [62]
		1 ML	3.25 Ref. [74]	0.10 Ref. [74]	0.002 Ref. [74]
	Cu	0.25 ML	2.63 Ref. [62]	0.48 Ref. [62]	−0.027 Ref. [62]
		1 ML	2.98 Ref. [74]	0.13 Ref. [74]	−0.003 Ref. [74]
F_s center	Ag	0.25 ML	1.81 Ref. [62]	2.12 Ref. [62]	0.32 Ref. [62]
			1.84 Ref. [48]	2.24 Ref. [48]	−0.3 Ref. [48]
		1 ML	$1.83/2.87^b$ Ref. [19]	0.80^c Ref. [19]	$0.30/0.011^b$ Ref. [19]
	Cu	0.25 ML	1.62 Ref. [62]	2.36 Ref. [62]	0.41 Ref. [62]
			1.66 Ref. [48]	2.43 Ref. [48]	−0.3 Ref. [48]
		1 ML	$1.64/2.32^b$ Ref. [19]	1.05^c Ref. [19]	$0.39/0.005^b$ Ref. [19]

[a] A positive sign means excess of the electron density as compared to a neutral atom.
[b] Optimized values for adatom positions above F_s center and O^{2-} ion.
[c] Averaged value of energy for monolayer adsorption per adatom.

nucleate d-metal islands is strongly element-dependent: to the right in a period, where d-shell filling is substantial, vacancies typically inhibit nucleation, whereas the opposite holds for far-left elements.

Our derived Mulliken charges on metal adatoms (copper and silver) over regular and defective MgO(001) substrates obtained in the DFT-LCAO calculations [62] show negligible interfacial charge transfer on the defect-free magnesia substrate. The electron density redistributions for a 0.25 ML of Cu and Ag over O^{2-} ions [Figs. 2(a) and (b)] show that Cu atoms are more strongly polarized by the substrate than Ag atoms, which results in stronger bonding of Cu atoms to the substrate than Ag (0.62 eV vs. 0.40 eV per adatom, Table I). For copper and silver atom adsorption over a defective substrate, we found noticeable electron charge transfer (~0.5 e) from defect to the Me adatom above it [Figs. 2(c) and (d)], thus forming a pair of oppositely charged defects, $Me^{\alpha-}/F_s^{\beta+}$ (α = 0.41 e vs. 0.32 e and β = 0.42 e vs. 0.34 e for Cu and Ag, respectively) [62]. As a result, Cu atoms are also more strongly bound over the F_s centers than Ag atoms (2.36 eV vs. 2.12 eV per adatom) and the length of a $Cu^{\alpha-}$—$F_s^{\beta+}$ bond is shorter by 0.19 Å (Table I). Nevertheless, the Mulliken population of the $Me^{\alpha-}$—$F_s^{\beta+}$ bond is found to be larger for Ag (0.33 e vs. 0.25 e for Cu).

For 1 ML metal adlayer coverage, the difference between the interfacial bonding on regular and defective substrates is found to be even more evident. Table I illustrates that in the former case, metal adatoms are markedly more weakly bound than for 0.25 ML [cf. Figs. 2(a) and (b) with 3(a) and (b)]. This confirms the metal atom's ability to form 3D clusters on a defect-free substrate as predicted thermodynamically (the stronger the metal atoms are bound to the MgO (001) surface, the lower is their ability for clusterization [73, 85]). For 1 ML coverage on a defective substrate [Figs. 3(c) and (d)], the conclusion can be drawn that although the metal adatom is strongly bound to the O vacancy, in fact it mimics the ion, and the surrounding atoms are only slightly affected by the presence of the defect as compared with defect-free surface [Figs. 3(a) and (b)]. The difference electron charge redistributions for 1 ML coverage of a defective substrate by Cu and Ag [Figs. 3(c) and (d)] clearly show that instead of metallic bonding between the Ag (Cu) atom, adsorbed above the oxygen vacancy, and those positioned over the neighboring surface oxygen ions, additional polarization appears between the latter adatoms and defective substrate, which leads to a larger stability of the 2D adlayer as compared with the defect-less interface. (Again, for Cu, this effect is
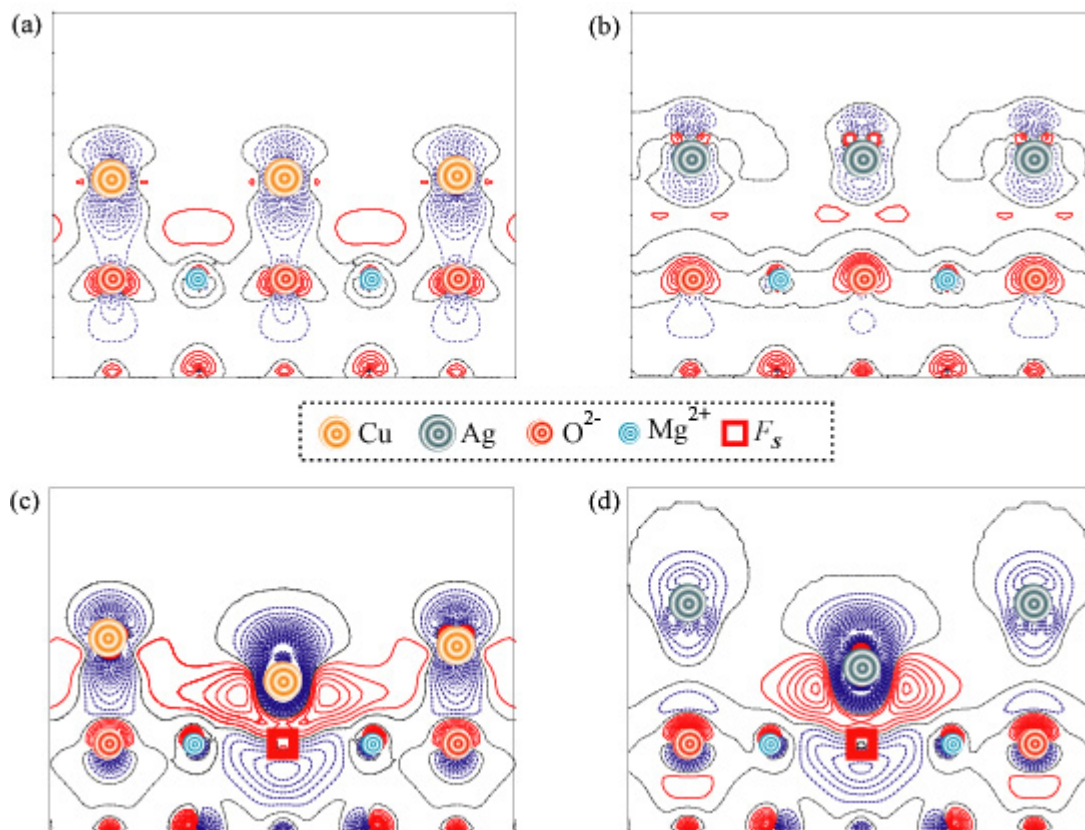
FIGURE 3. 2D difference electron density plots projected onto the (100) section plane of MgO (see Fig. 1) for its 1 ML coverage by: (a) Cu and (b) Ag over regular (001) surface as well as (c) Cu and (d) Ag over defective surface containing F_s center regularly distributed with a 0.25 ML periodicity [19]. See caption of Figure 2 for explanation of other details of plots. [Color figure can be viewed in the online issue, which is available at www.interscience.wiley.com.]

found to be more pronounced than for Ag.) Thus, we confirmed the conclusion [87b] that F_s centers on the MgO(001) substrate prevent adatom nucleation for transition metals with a small d shell electronic population. The calculated critical defect concentration for 3D → 2D transition in Cu film growth mechanism on the substrate is markedly smaller than that for Ag (10 vs. 40%, respectively [95]). Experimental confirmation of these predictions by means of surface irradiation would be of great interest.

3.2. ALUMINA

Another "classical" material widely used for defect studies in binary oxides is corundum (sapphire) or α-alumina [Al_2O_3] prized for its hardness, optical transparency, refractory character, large

band gap, and applied as a substrate for surface overlayer growth, thus being used in many technological applications [8]. Besides the thermodynamically most stable α-alumina form, Al_2O_3 exists also in a number of metastable phases (*transition* aluminas [96]), widely used in catalysis, microelectronics, optics, etc., and being the subject of numerous experimental and theoretical investigations [97]. The transition aluminas are derived by thermal dehydration of aluminum hydroxide precursors. One of four main dehydration sequences, boehmite → γ → δ → θ → α phase transitions [98], is of particular interest since γ-Al_2O_3 is one of the most important catalytic support materials. Nevertheless, we consider in this review only defects in corundum (both bulk and (0001) surface) as the simplest alumina.

Each O atom in a corundum crystal is surrounded by four Al atoms (Fig. 4), forming two
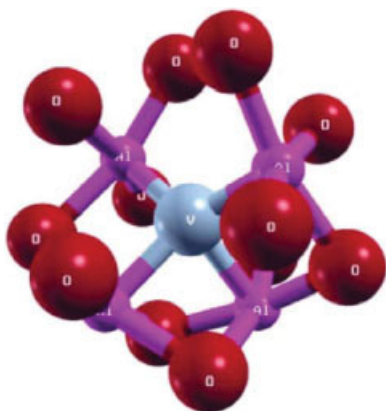
FIGURE 4. The local environment of the oxygen vacancy (*V*) in bulk α-Al$_2$O$_3$. Four Al nearest ions and 12 next-nearest O ions are shown. Note that two of four Al neighbors are located closer to oxygen vacancy than other two, the same is true for oxygen neighbors. [Color figure can be viewed in the online issue, which is available at www.interscience.wiley.com.]

kinds of Al—O bonds with the lengths of 1.86 and 1.97 Å, as well as 12 next-nearest oxygens [98]. The α-Al$_2$O$_3$ crystallizes in a rhombohedral structure, with space group $R\bar{3}c$ (D_{3d}^6), and lattice parameter a_0 = 5.13 Å and α = 55.33°. The hexagonal setting (with a and c lattice parameters) is also widely used for description of corundum [99]. The oxygen atoms form a hexagonal close-packed structure while the aluminum atoms regularly occupy 2/3 of the octahedral interstitials. Unlike alkali halides and alkali earth oxides, creation of the *F* center in corundum crystal results in a substantial lowering of a local symmetry ($D_{3d}^6 \rightarrow C_2$). Probably, the noticeably smaller number of theoretical simulations on oxygen vacancies in α-Al$_2$O$_3$ [3, 7, 9, 10, 100–106] may be explained by this low-symmetrical structure and, thus, complexity of calculations required significant computational time and resources as well as interpretation of their results [102]. The following methods and models were used for the *F* center studies in corundum: (i) periodic DFT calculations [9, 10, 100–104]; (ii) time-dependent (TD) DFT calculations on embedded clusters [7, 104] using the GAUSSIAN code [107]; (iii) semi-empirical embedded [3, 105] and cyclic [9, 106] cluster calculations by the INDO and MSINDO methods, respectively. Phenomenological description of the oxygen vacancies in alumina through analysis of their diffusion was given in Ref [108].

3.2.1. Corundum Bulk

The *F* center in the ground state of α-Al$_2$O$_3$ bulk, similarly to MgO, produces a deep level (occupied by two electrons) at 2.3 eV above the top of VB, as found in the periodic DFT PW calculations [102]. Qualitatively similar results were also obtained in other periodic DFT calculations: 2.0 eV [103] and 3.4 eV [100], whereas the semi-empirical methods usually overestimate this value: 5.3 eV in INDO embedded cluster calculations [105]. The band gap width (experiment suggests 8.75 eV [109]) is noticeably underestimated in the DFT PW calculations: 5.9 and 7.2 eV for PWGGA *xc*-functional combined with either the projected augmented wave (PAW) or ultrasoft pseudopotential (US PP) implemented in the VASP code [103]. (This difference shows noticeable dependence of results on hidden DFT parameters, while using the same periodic model.) The periodic DFT-B3LYP calculations give 8.5 eV [110], whereas both the TD-DFT embedded cluster calculations [104] and semi-empirical INDO cluster calculations [105] overestimate this value: 9.9 and 10.1 eV, respectively.

Unlike the well known localized character of electrons trapped by the *F* center in bulk MgO, little is known about the electronic structure of these defects in α-Al$_2$O$_3$. The semi-empirical INDO method applied to an Al$_{26}$O$_{39}$ stoichiometric cluster indicates that the wave functions in the ground state are well localized within the vacancy, thus confirming results of the population analysis of the Al—O bonds indicating partial covalency [105]. However, this contradicts Hartree–Fock studies which show almost complete ionic character of corundum bonding [111]. Such a discrepancy could be attributed to two effects: the neglect of the Madelung potential in the INDO cluster and the use of empirical parameters.

Formation of the *F* center is accompanied by a reduced symmetry (local C_2 point group) and relaxation of the surrounding ions. Unlike the oxygen vacancy in magnesia, theoretical results obtained for corundum are quite controversial: (i) in the periodic DFT calculations on the rhombohedral supercells the inward relaxation of the two Al ions nearest to the *F* center are -4.5 to -5.5%, the two more remote Al ions were found to be slightly shifted outwards (by $+0.6$ to $+0.9\%$) whereas the next-nearest O neighbors are negligibly relaxed inwards, by -0.1 to -0.6% [103]. A qualitatively similar relaxation was also observed in other DFT-PW and TD-DFT calculations [102, 104] (ii) in the semi-

empirical INDO (embedded cluster) [105] and MSINDO (cyclic cluster) [106] calculations, the direction of relaxation of Al ions nearest to a vacancy was found to be quite opposite: +2.8 and +1.8% for the nearest and next-nearest Al ions as well as +2.2% for oxygen neighbors [105] vs. +0.5 and +4.0% for both types of Al neighbors and small inward shift (−0.4%) for the nearest oxygens [106].

The VASP calculations of the F center using a $3\times3\times1$ hexagonal supercell (with the nearest inter-defect distance $d_{F-F} \approx 9$ Å) have shown negligible repulsion of the nearest vacancies [10, 103]. The formation energy of a single oxygen vacancy in these calculations [103] was found 10.3 and 9.3 eV, as computed within the PWGGA [34] and PBE [35] functionals, respectively. This again demonstrates an intrinsic uncertainty of both methods including different ways to estimate the energy of atomic oxygen. The nearest Al ions relaxed here inwards, by about 5%, and the nearest O ions also inwards, but only by 0.6%. The results of the periodic DFT-PW calculations [102], treated using a standard thermodynamic formalism by Zhang and Northrup [112], have shown the dependence of the formation energy on the oxygen chemical potential: E^{form} increases from 8 to 12 eV as $\Delta\mu_O$ increases from −2 to 0 eV. The MSINDO cyclic cluster calculations result in the value of 11.8 eV [106], so these data are close for different methods and models used (except for 5.8 eV in earlier LDA-PW calculations [100] found to be rather controversial when compared with results obtained in GGA-PW studies [101–103]). In any case, since experimental data for the formation energy are still absent, the only criterion can be a certain proximity with the F center formation energy in MgO bulk considered in Section 3.1.1.

Determination of position of the saddle point on the *diffusion* path of a vacancy in corundum bulk is a nontrivial problem due to a possibility of five migration paths [113]. Nevertheless, the value of 3.7 eV [10] calculated by VASP for a periodic model is not too far from the experimental value of 4.5 eV [114]. To rationalize the trend in the diffusion barrier for oxygen vacancies in ionic oxides, the calculated diffusion energy was earlier plotted as a function of the Madelung potential at the saddle point obtained from the Ewald summation, assuming formal charges for all ions in the crystal [105]. In that way the migration energy was described as a function of the ionic radii and the ionic charges.

F centers are believed to be the most stable defects in binary oxides, with the characteristic absorption spectra [103]. The optically excited state of the F center in α-Al$_2$O$_3$ bulk ($1A \rightarrow 2A$, which corresponds to the excitation of s-like orbital strongly localized in the oxygen vacancy to p_z-like orbital also localized in the cavity but exhibiting a nodal plane leads to electron density in the region near the second shell) is close to the conduction band bottom [3]. Its experimental energy (6.05 eV [115]) was reasonably well reproduced in both semi-empirical INDO embedded cluster calculations (5.9 eV [3, 105]) and first-principles TD-DFT embedded cluster calculations (6.16–6.19 eV [104]). As to periodic models, they cannot be properly used for the description of localized excited and charged defects.

3.2.2. The (0001) Corundum Surface

Surfaces of the many alumina phases important as catalytic supports [96–98], are difficult to characterize since they are less stable than the α-Al$_2$O$_3$ (0001) substrate, both energetically and structurally. Thus we consider here mainly the corundum (0001) surface which is well suited for both measurements and computer simulations [116], also with the oxygen vacancies [103, 104]. Tasker's classification for ionic crystalline compounds [57] also gives a preference for the (0001) face as the most densely packed and energetically stable among other corundum surfaces (such as (11$\bar{2}$0), which was also simulated [117]). Both aluminum- and oxygen-terminated polar α-Al$_2$O$_3$ (0001) surfaces can exist, depending upon preparation conditions [116]. The Al-terminated surface is stoichiometric, being close to the corundum bulk structure, and energetically stable [118]. However, the O-terminated surface possesses the higher reactivity and can be stabilized by either metal deposition [119] or hydroxylation [120].

A common feature of all theoretical studies is the prediction of a marked Al-terminated corundum (0001) surface relaxation, especially for the outermost Al atomic layer. The surface relaxation involves many atomic layers, and moreover, we have shown that the outer atomic layers undergo a quite complex relaxation involving not only the vertical relaxation, but also a rotation-like displacement of the oxygen atomic layers [118, 119].

The first theoretical studies of surface oxygen vacancies on the Al-terminated corundum (0001) surface were performed only recently [103, 104]. This surface may be regarded as a sequence of Al-O-Al-Al-O-Al. . . layers and therefore one can distinguish two different types of surface oxygen

atoms: those in the second layer and in the fifth layer. Both cases have been considered; however, no low-coordinated oxygen vacancies have been studied. The periodic PWGGA [33] derived formation energies for O vacancy were found to be 8.9 and 9.5 eV in the 2nd and 5th layers, respectively. The former is noticeably lower than that obtained for the oxygen vacancy in corundum bulk (see Section 3.2.1). The contribution of lattice relaxation to the energy gain is almost an order of magnitude larger that in the bulk, i.e., 0.44 and 0.37 eV for the F_s center (2nd and 5th layers). In the TD-DFT embedded cluster calculations the vacancy formation energy on corundum surface was 6.9 eV, i.e., ~2 eV smaller than in periodic calculations [104]. There are structural differences between surface and bulk vacancies; for the O vacancy in the second layer, there are three neighboring Al atoms: the external nearest neighbor moves inwards by 13% and the two internal neighbors outwards, by ~1% (nearest) and 6% (next-nearest). For the F_s center in the fifth corundum (0001) layer, there are four neighboring Al atoms and all relax outwards, at variance with the bulk and subsurface vacancy: 2.0 and 2.5% for the nearest and 4.0 and 5.6% for the next-nearest neighbors, respectively. This result shows that, contrary to simple oxides such as MgO, the 5th atomic layer is still far from exhibiting bulk properties and indicates that, for certain purposes, the use of thin slabs or small cluster models of α-Al$_2$O$_3$ (0001) should be avoided or used with extreme care [103]. Notice that there is a considerable difference between the chemical nature of MgO (001) and α-Al$_2$O$_3$ (0001) surfaces: the former is neutral and the latter polar.

The TD-DFT electronic structure calculations carried out on a properly embedded cluster model [104] with the correct geometric structure and the vacancy relaxation (obtained from periodic supercell calculations) allow the calculation of optical transitions for the bulk and surface F and F^+ point defects in α-Al$_2$O$_3$. The difference between the band positions for surface F_s and F_s^+ centers (as compared to the top VB) is 0.3 eV smaller than for the bulk centers [104].

Since the formation energies of oxygen vacancies in corundum bulk and on the (0001) surface are semi-quantitatively similar to those for MgO bulk and the (001) surface, it could be expected that the polar α-Al$_2$O$_3$ (0001) surfaces play an important role as nucleation centers of supported metals on corundum and exhibit a rich chemistry, similar to that reported in Section 3.1.3 for oxygen vacancies

on the non-polar MgO (001) surface. There exist numerous theoretical studies on the perfect interfaces between different transition metals (Ag, Cr, Cu, Nb, Pd, Pt, and Rh) and an alumina substrate [119–129]. By combining the DFT-PW and DFT-LCAO calculations, we have studied the ionic conductivity at the AgCl/α-Al$_2$O$_3$ (0001) interface with a reduced amount of interfacial silver ions atop the regular Al-terminated substrate [130]. Despite the calculated low activation energy for Ag vacancy transport in the interfacial layer (0.23 eV), the vacancy concentration is too small for generating perceptible surface conductivity. However, we found no references on first principles simulations of these interfaces with surface F_s centers (only the influence of surface OH-groups on interfacial properties [120, 127, 129] was studied). Thus, qualitative conclusions of Section 3.1.3 can be inferred, in expectation of the future calculations on defective Me/α-Al$_2$O$_3$ (0001) interfaces.

4. Defects in Ternary ABO$_3$ Oxides of Transition Metals

Perovskite oxides have received considerable attention as materials for solid oxide fuel cells, catalytic and electrochemical applications, hydrogen membranes and sensors, etc. [5]. For example, some of these oxides are catalytically active in the oxidation of CO and reduction of NO in automobile exhaust reduction. Mixed oxides with the ABO$_3$ perovskite structure are flexible systems as their properties can be adjusted or enhanced for specific applications by chemical doping at the A or B cation sites. Alternatively, these oxides can also contain defects in the form of electron holes or traps depending on the type of the B cation site and the nature of the dopant.

ABO$_3$ compounds comprise a rich family of crystalline structures and their mixtures [1–5]: simple cubic [Fig. 5(a)], tetragonal, orthorhombic, etc. which result in existence of ferroelectric, antiferroelectric, and other phases with specific, technologically important properties. Under different external conditions (temperature, pressure, etc.) practically each perovskite oxide can exist in different crystalline phases, and the corresponding phase transitions can drastically change its physical and chemical properties as well as the area of applications.

In spite of substantial efforts, the nature of many defects in ABO$_3$ perovskites is rather unclear since
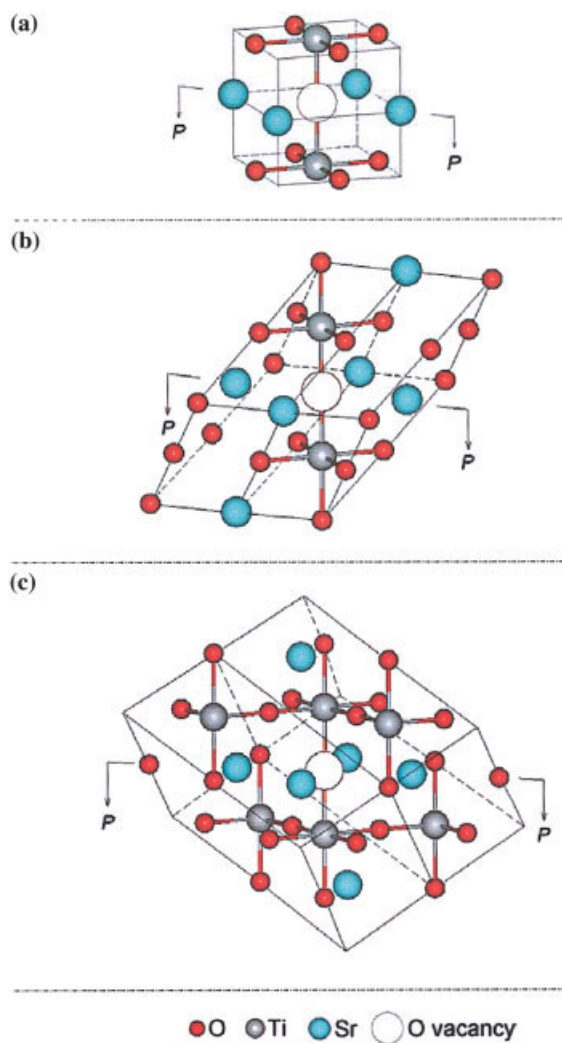
FIGURE 5. Three types of equidistant crystalline cells with a centered O vacancy for the cubic phase of Sr-TiO$_3$ perovskite: (a) simple cubic (*sc*); (b) face-centered cubic (*fcc*); (c) body-centered cubic (*bcc*). Sticks between the oxygen and titanium ions indicate the partly covalent bonds between them. To construct the difference electron density plots shown in Figure 6, supercells are sectioned along the —Ti—O—Ti— axis by the plane *P–P*. [Color figure can be viewed in the online issue, which is available at www.interscience.wiley. com.]

their electronic structure exhibits an increased complexity, which hinders a proper characterization. In most previous simulations of oxygen vacancies in ABO$_3$ perovskites, the simple cubic paraelectric phase was considered [3, 5, 7, 8, 18, 131–150]. This is true for defective SrTiO$_3$ whose structure is cubic at room temperature (RT) whereas for other perovskites this is usually a high-temperature phase. Nevertheless, the *F* centers were also studied in the low-temperature antiferro-distortive (AFD) tetragonal phase of SrTiO$_3$ [133, 138], as well as in both ferroelectric RT-stable tetragonal phases of PbTiO$_3$ [5, 142, 150–152], BaTiO$_3$ [5, 143], and the orthorhombic phase of KNbO$_3$ [3, 144–146, 150, 153] perovskites. Various computational methods were used to model *F* centers in ABO$_3$ perovskites: (i) periodic DFT-PW [18, 131, 134, 136–142, 151, 152] and DFT-LCAO [18, 140, 141, 147] calculations; (ii) periodic large unit cell (LUC) semi-empirical INDO calculations [133, 135, 143–146, 148–150, 153], as well as (iii) DFT-LCAO and HF calculations on embedded clusters [5, 132, 136]. The latter clearly show that in building up a quantum cluster, which requires breaking of the covalent bonds between atoms, the Coulomb embedding potential is rather insufficient and a more sophisticated cluster model is needed [7].

The *F* center in perovskites resembles on the *E'* centers (Si dangling bonds) formed in several oxides and silicates, where each O ion is surrounded by only the two nearest neighbor positive cations [7], rather than the *F* centers in MgO-type ionic solids where two electrons are strongly localized by the Madelung field in the O vacancy. However, the analogy with *E'* centers is not complete since this should lead to the creation of Me—Me bonds and strong displacements of both Me ions towards each other. Thus, O vacancies in perovskites really cannot be attributed to earlier defined type of centers; yet for simplicity we continue to call them the *F* centers.

4.1. TITANATES

The Ti-containing ATiO$_3$ ternary oxides are the most comprehensively studied perovskites, both experimentally and theoretically [1, 2, 5, 8, 18, 131, 133–143, 148–152]. Their properties depend mainly on well-studied partly covalent-bound Ti—O substructure where Ti and O ions are nearest neighbors. Combined with the predominantly ionic A—O bonds (A = Sr, Ba, Pb, Ca), this mixed nature of the chemical bonding leads to a unique ionic-covalent electronic structure of ATiO$_3$ perovskites [149], irrespective of which crystalline phase (cubic, tetragonal, orthorhombic) is considered. Creation of an oxygen vacancy markedly changes the electronic states of the two titanium atoms (mainly in their *3d* orbitals) on both sides of the defect. In any case, the partly covalent

chemical bonding makes simulation of *F* centers in titanates a rather complicated problem, even in the cubic phase.

4.1.1. SrTiO$_3$ Bulk

In this Section we mainly present results of our own oxygen vacancy simulations in the cubic structure of strontium titanate [18, 140, 141], which are compared with data from other studies. The results obtained for the AFD structure (slightly distorted cubic phase comprehensively described recently [154], stable at temperatures below 105 K) containing oxygen vacancies [133, 138] are discussed at the end of the Section. The theoretical study of *isolated* single defects is not only nontrivial and time consuming but remains an important issue, since in many experiments the defect concentrations are quite low. Most calculations performed so far corresponded to unrealistically high defect concentrations, which thus do not permit a direct comparison with experiments [141]. Thus, we analyzed the approach to a limit of single defect in our periodic models of cubic SrTiO$_3$ perovskite containing *F* centers.

The simple cubic (*sc*) structure of perfect SrTiO$_3$ has the space group $Pm\bar{3}m$ (local group C_{4h}). However, in order to place the coordinate origin on an O vacancy, we use the $P4/mmm$ space group with the same C_{4h} local symmetry at the *F* center [Fig. 5(a)]. Both DFT-LCAO and DFT-PW calculations have been performed by us for defective supercells of different shapes and sizes, created by the following:

i. equidistant extension of the lattice vectors [18]: face-centered cells $2\sqrt{2} \times 2\sqrt{2} \times 2\sqrt{2}$ (80 atoms *per* supercell) and $3\sqrt{2} \times 3\sqrt{2} \times 3\sqrt{2}$ defective (270 atoms), simple cubic cells $3 \times 3 \times 3$ (135 atoms) and $4 \times 4 \times 4$ (320 atoms), as well as a body-centered cell $2\sqrt{3} \times 2\sqrt{3} \times 2\sqrt{3}$ (160 atoms); the corresponding *sc-*, *fcc-*, and *bcc*-extensions of the SrTiO$_3$ unit cell shown in Figures 5(a)–(c) are described by the transformation matrices defined in Eq. (1), see Section 2.1:

$$\begin{vmatrix} n & 0 & 0 \\ 0 & n & 0 \\ 0 & 0 & n \end{vmatrix}, \quad \begin{vmatrix} 0 & n & n \\ n & 0 & n \\ n & n & 0 \end{vmatrix}, \quad \text{and} \quad \begin{vmatrix} -n & n & n \\ n & -n & n \\ n & n & -n \end{vmatrix},$$

(5)

respectively, where *n* is varied between 2 and 4;

ii. non-equidistant extension of the lattice vec-

tors [140] due to anisotropy in the Ti—O—Ti direction for atomic relaxation around the *F* center: $2 \times 2 \times n$ ($n \leq 7$), $3 \times 3 \times n$ ($n \leq 5$), and $4 \times 4 \times 3$ containing up to 240 atoms *per* supercell.

Our studies [18, 140, 141] have clearly demonstrated the advantage of combining DFT-PW and the DFT-LCAO calculations, which allow us to obtain quite complementary results. For example, the optical gap in the BZ was found to be 3.65 eV for hybrid B3PW *xc*-functional in DFT-LCAO calculations, quite close to the experiment (3.25 eV for the indirect band gap [155]). At the same time, the DFT-PWGGA calculations (in the framework of the VASP code, and, in general, for all GGA methods) predict a significantly underestimated value of 2.1 eV which can affect the electronic structure of the oxygen vacancy. Thus, we are more confident in estimating position of the defect level with respect to the CB bottom when performing the DFT-LCAO calculations. The *F* center energy level in the band gap approaches the CB bottom (being separated by $\Delta\varepsilon_{db\text{-gap}}^{\Gamma}$ from it), moving from 0.69 eV for an 80-atom supercell (with the defect bandwidth of 0.15 eV), down to 0.57 eV (0.08 eV) for 160-atoms, and reaching finally the optical ionization energy of 0.49 eV (with almost negligible bandwidth of 0.02–0.03 eV) for 270- and 320-atoms with the defect period close to four lattice constants (Table II). Achieving the convergence with the supercell increase up to 270–320-atoms, the defect–defect interaction becomes negligible, thus approaching a realistic model of a *single F* center, similar to the study of Fe impurities in SrTiO$_3$ [28]. Since the commonly accepted experimental estimate of the neutral *F* center ionization energy indicates a shallow defect [155], very close to the CB bottom, we suppose that the remaining discrepancy can be explained by the overestimated band gap in DFT-LCAO calculations (by 0.4 eV as mentioned earlier). It also means that previous calculations performed for cubic SrTiO$_3$ with *F* centers, using $2 \times 2 \times 2$ and $3 \times 3 \times 3$ extended supercells [131, 133–137, 139, 140, 148] described the O vacancy electronic structure insufficiently correctly.

Other structural and electronic properties of defective cubic SrTiO$_3$ bulk were also analyzed in the limit of a single *F* center. Our DFT-PW calculations on 270- and 320-atom SrTiO$_3$ supercells give a reasonable estimate for the vacancy formation energy, $E^{form}(F) = 7.1$ eV [18] whereas the same calculations on different $m \times m \times n$ square parallelepipeds give a convergence limit of the 7.2 eV [141]. These for-

TABLE II

Dependence of lattice relaxation for the nearest equivalent atoms around F center in a cubic $SrTiO_3$ crystal on both shape (Fig. 5) and size of supercells used in DFT-PW (VASP) calculations [18, 141].

Atoms nearest to F center	Unrelaxed distance from F center, a_o	Unrelaxed coordinates			Number of atoms shifted equivalently	Relative shifts δR_i from unrelaxed positions[a] (%)		
		x_i	y_i	z_i		160-atom SC, bcc	270-atom SC, fcc	320-atom SC, sc
Ti	$a_o/2$	0	0	$\pm a_o/2$	2	7.08	8.28	7.76
O	$a_o/\sqrt{2}$	$\pm a_o/2$	0	$\pm a_o/2$	8	-7.98	-7.43	-7.79
		0	$\pm a_o/2$	$\pm a_o/2$				
Sr	$a_o/\sqrt{2}$	$\pm a_o/2$	$\pm a_o/2$	0	4	3.45	3.42	3.94
O	a_o	$\pm a_o$	0	0	4	2.49	2.87	3.56
		0	$\pm a_o$	0				
O	a_o	0	0	$\pm a_o$	2	-1.67	-1.05	-1.28

[a] Positive shift corresponds to expansion of the atomic coordination sphere whereas negative sign means its compression.

mation energies are 2.5–3.0 eV smaller than those for α-Al_2O_3 and MgO bulk (Section 3) which can be attributed to the different nature of bonding (a similar value of 7 eV was found also for ionic-covalent ZnO [10]).

The strong relation between the defect formation energy and the local lattice relaxation has already been observed for other covalent oxides. The sensitivity of calculated lattice relaxation around defect to both the supercell shape and size is also clearly seen in Table II. For a given type of superlattice (*sc, fcc,* or *bcc*), an expansion of the first coordination sphere (two Ti ions) is larger (7.1–8.3%) whereas a compression of the second sphere (eight O ions) is only slightly smaller (7.4–8.0%) [18]. The relaxation of the next two coordination spheres around the F center is also substantial (1–4%). This confirms the necessity to consider as large supercells as possible, to take into account all atomic relaxations which are seen converge slowly with an increase of the distance from the oxygen vacancy. This is well correlated with results of other DFT-PW calculations on a 4×4×4-extended supercell [138]. Meanwhile, the nature of the lattice relaxation here is complex and anisotropic, depending also on both supercell size and shape (Table II). For instance, *fcc* supercells are stretched along the z axis and compressed in the xy-plane [Fig. 5(b)]. This causes larger z-shifts of Ti ions nearest to O vacancy in 270-atom *fcc* supercells as compared with 160-atom *bcc* and 320-atom *sc* supercells, whereas xy-shifts of the nearest O and Sr ions are smaller in the former case.

The DFT-PW calculations of the energy barrier for oxygen vacancy diffusion in $SrTiO_3$ bulk shows a non-linearity of the O migration path through the middle of Sr-Ti-Sr triangle [Fig. 5(a)] and resulted in $E^{diff}(F) = 0.4$–0.5 eV, depending on the supercell size and shape. This is smaller than the experimental estimate of 0.86 eV [157]. However, special care must be taken when comparing theory with experiment since the experiments were performed at high temperature when the F centers have already released their two electrons to the conduction band [156]. This is consistent with empirical shell model calculations for the empty O vacancy in a cubic $SrTiO_3$ crystal which predict the migration barrier of 0.76 eV [158], closer to experiment. The energy barrier for oxygen vacancy diffusion in $SrTiO_3$ bulk is almost an order of magnitude smaller than that in MgO and α-Al_2O_3 bulk [10], which indicates an energetic preference of perovskites favorable for defect transport engineering.

The formalism of Wannier functions applied recently for the determination of effective charges and bond populations in several pure perovskite crystals including $SrTiO_3$ [159] gives the atomic charge of $+2.55$ e on titanium and -1.55 e on oxygen, whereas the Ti—O bond order is 0.35 e. The charge on Sr ($+1.95$ e) is close to the nominal ionic value $+2$ e confirming its ionic bonding. According to our recent DFT-LCAO calculations on the cubic phase of $SrTiO_3$ perovskite [140], a Mulliken effective electronic charge of 1.1–1.3 e is localized in the neutral O vacancy (depending on the supercell size) and 0.6–0.8 e are equally shared between the two nearest Ti ions. The Bader topological charge anal-
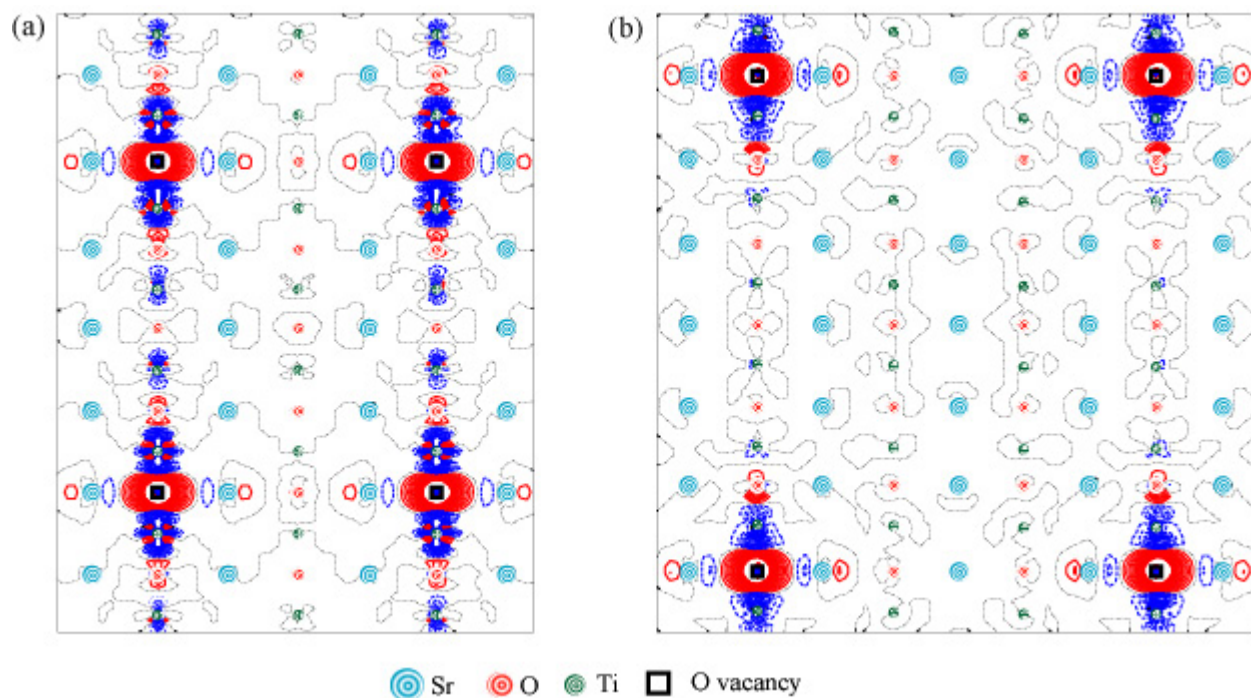
FIGURE 6. 2D difference electron density plots projected onto the (110) section plane *P–P* (Fig. 5b) for 80-atom (a) and 270-atom (b) *fcc* supercells containing a single oxygen vacancy [18]. Isodensity increment is 0.003 *e* Å^{-3}. See caption of Figure 2 for explanation of other details of plots. [Color figure can be viewed in the online issue, which is available at www.interscience.wiley.com.]

ysis of DFT-PW calculations usually underestimates charge transfers in perovskites: -1.2 *e* (O), $+2.0$ *e* (Ti), and $+1.6$ *e* (Sr) [141]. The redistribution of the electron density induced by the O vacancy formation is shown in Figures 6(a) and (b) as calculated for the equidistant *fcc* supercells with different extensions. Comparison of both plots clearly shows the marked decrease of induced inter-defect redistribution of the electron density as the supercell increases from $2\sqrt{2}\times2\sqrt{2}\times2\sqrt{2}$ (80 atoms) up to $3\sqrt{2}\times3\sqrt{2}\times3\sqrt{2}$ (270 atoms).

So far, only two theoretical studies were reported for the *F* center in low-temperature tetragonal and RT cubic phases of strontium titanate [133, 138]. The DFT-PW calculations have shown that the relative stability of the AFD phase over the cubic phase of SrTiO$_3$ (since the calculations were performed at 0 K) substantially decreases in the presence of oxygen vacancies. This is in agreement with a recent experimental study [160] which found that T_c for the cubic to AFD phase transition drops from 105 K to near 98 K for samples with higher (approx-

imately two orders of magnitude) *F* center concentrations. Comparison of the charge redistributions and atomic distortions near the vacant site for both cubic and AFD phases shows that in the presence of an oxygen vacancy, the local atomic structures and charge densities are quite similar. In a sense, the energy gain of the AFD phase over the cubic phase by the rotation of the TiO$_6$ octahedra along a particular direction is locally replicated by an oxygen vacancy in the cubic phase while still maintaining a D_{4h} symmetry [138]. Hence, the cubic phase becomes more competitive with the AFD phase in lowering T_c. Semi-empirical INDO calculations suggest that the electrons are not strongly trapped by the O vacancy in the tetragonal phase as compared with cubic SrTiO$_3$ [133].

4.1.2. The SrTiO$_3$ (001) Surface

There exist several theoretical studies of perovskite-structured SrTiO$_3$ (001) surface relaxation for the two different terminations (SrO and TiO$_2$) per-

formed using ab initio HF [161, 162], hybrid DFT-LCAO [162, 163], and DFT-PW [164–166] methods, the semi-empirical INDO method [135] and atomistic methods based on the shell model [167, 168]. Marked increase of Ti—O bond covalency nearby the surface and energy gap reduction, especially for the TiO_2 termination, were found [161–163]. Structural relaxation and longitudinal dipole moments of $SrTiO_3$ (001) and (110) surfaces were studied in Ref. [165]. For the $SrTiO_3$ (001) surface, the LEED (low-energy electron diffraction), RHEED (reflection high-energy electron diffraction), STM (scanning tunneling microscopy), and SXRD (surface X-ray diffraction) studies have revealed numerous reconstructions under different conditions: (1×1), (2×1), (2×2), $c(4\times2)$, $c(6\times2)$, and $(\sqrt{5}\times\sqrt{5})$ $R26.6°$ [169]. In direct refinements of SXRD data [170] some $SrTiO_3$ (001) surface reconstructions are characterized by an additional TiO_2 overlayer on top of an already TiO_2-terminated (001) surface (double layer, DL) which destroys *substrate stoichiometry*. A thermodynamic stability diagram obtained from our recent hybrid-DFT calculations [171] shows, however, that regular TiO_2- and SrO-terminated (001) surfaces are still the most stable. Our simulations show also a substantial increase of Ti—O covalency on the DL surfaces as compared with the regular (001) surfaces, which are themselves more covalent than bulk.

The knowledge of atomic and electronic structure of strontium titanate surface F_s centers is rather scarce [131, 135, 141, 148]. Moreover, in most of these papers [131, 135, 148] the F_s centers were modeled at unrealistically high concentrations; also, no surface defect migration energies were presented. In a recent paper [141], we have studied surface F_s centers on the TiO_2-terminated unreconstructed (001) surface. This choice is motivated by its abundance at normal air pressures and its common nature for all titanium perovskites. A stoichiometric slab containing six atomic TiO_2 and SrO planes has been chosen as a material model. The formation energies for relaxed surface oxygen vacancies are 6.22 eV for 120-atoms and 5.94 eV for 270-atom supercells with $2\sqrt{2}\times2\sqrt{2}\times3$ and $3\sqrt{2}\times3\sqrt{2}\times3$ extensions, respectively. The conclusion could be drawn that the defect formation energy on the TiO_2-terminated surface is considerably smaller than in the bulk; it is reduced by ~1.5 eV or ~20–25% for supercells containing the same number of atoms (270). This is similar to what was obtained for other oxides and it is due to a reduced O coordination at the surface (Section 3). The relaxation of the Ti and
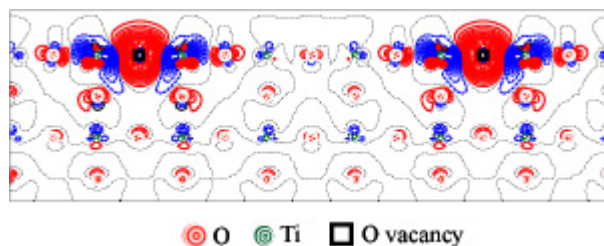

FIGURE 7. 2D difference electron density plots projected onto the (100) cross section of the difference electron density map for the 120-atomic sixth-layer slab supercell [142]. See caption of Figure 2 for an explanation. [Color figure can be viewed in the online issue, which is available at www.interscience.wiley.com.]

O atoms nearest to the F_s center are 14% (outwards) and 8% (mainly inwards), respectively, thus exceeding by a factor of 1.5–2.0 those in the bulk (The nearest oxygen atoms move inwards along the surface and outwards across it). Atomic displacements in the smaller 120-atom supercell show a nonmonotonic decay with the distance from the vacancy (e.g., surface oxygen atom separated from a vacancy by $2a_0$), which is caused by interference effects on the border of the neighboring supercells, demonstrating that this supercell is not big enough to avoid defect–defect interactions.

The calculated activation energy for defect migration along the surface for the two supercells of 120 and 270 atoms is 0.19 and 0.11 eV, respectively. This demonstrates that (i) a decreased defect concentration reduces the migration energy (because of reduced repulsion energy between periodically distributed defects), and (ii) as compared with the bulk, defect migration energy on the perovskite surface is largely reduced. This is in line with recent studies of F_s center migration on the MgO (001) surface (Section 3.1.2) where the activation energy was also considerably smaller than in bulk.

With respect to the electronic structure, Figure 7 presents the electron density redistribution due to vacancy formation at the TiO_2-terminated (001) surface. The difference electronic density plot for the surface F_s center concentration of 6.25% shows that the electronic density around vacancy is more delocalized than that for the bulk F center (Fig. 6). The calculated Bader effective charges of the two nearest Ti atoms give the electronic density increase of 0.4 e per atom, whereas the rest of the missing O charge is spread about in the vicinity of the vacancy (Fig. 6). The defect ionization energy $\Delta\varepsilon_{db\text{-gap}}^{\Gamma}$ of the F_s center (0.25 eV) is about half that in the bulk. This

is found for the 120-atom supercell, which is still far from convergence to the limit of a single defect. Here, the band dispersion is still not negligible (0.14 eV), being comparable with that for the bulk 80-atom supercell with extension $2\sqrt{2}\times2\sqrt{2}\times2\sqrt{2}$ (0.15 eV).

We disagree with the authors of periodic semi-empirical studies of surface oxygen vacancies on the $SrTiO_3$ (001) [135] and $SrTiO_3$ (110) [148] surfaces that eightfold or even fourfold-symmetric extension of the primitive unit cell is completely sufficient to reproduce correctly the electronic band structure of a given crystal (they considered 135- and 80-atom supercells modeling cubic and tetragonal phases, respectively). However, their conclusion that Ti atoms at the (110) surface are less positively charged as compared with the (001) surface agrees with both scanning microscopic and spectroscopic study [172].

Understanding of the initial stages of formation and growth of metallic overlayers on $SrTiO_3$ is important for microelectronic and optoelectronic applications [8]. However, only a few DFT-PW calculations on both SrO- and TiO_2- terminated stoichiometric unreconstructed $SrTiO_3$ (001) substrates with Pd [173–175] and Pt [175] overlayers were performed so far. Similarly to interfaces with binary oxides, the most preferable sites for adsorption of Pd and Pt atoms are found to be atop surface O ions. For greater coverage (≥1 ML), the interface between the Me overlayer and TiO_2-terminated substrate is more stable. However, the energetically preferable mode was found to be metallic *island growth* on this substrate unlike technically desirable layer-by-layer mode [174, 176]. Our simulations of Ag and Cu films growth on the regular MgO (001) surface [73, 85, 86] (Section 3.1.3) are in line with this conclusion. Previous studies of idealized Me/ $SrTiO_3$ interfaces must be complemented by modeling surface point defects, firstly, the F_s centers. We expect that these defects can qualitatively change the growth mode of thin metallic films.

4.1.3. BaTiO₃

The cubic phase of barium titanate is known to be stable at $T \gtrsim 400$ K, with decreasing temperature it usually undergoes a series of phase transitions to slightly distorted ferroelectric structures with tetrahedral, orthorhombic, and rhombohedral symmetry [177]. Ferroelectric $BaTiO_3$ perovskite, existing at RT in the tetragonal phase, is widely used in

multilayer capacitors, piezoelectric transducers, and nonlinear positive-temperature-coefficient resistors [178]. It also possesses large electro-optic coefficients and high photo-refractive sensitivity, therefore this perovskite can be used as an optical sensor [179]. The spectrum of $BaTiO_3$ applications was noticeably enhanced after synthesis of $Ba_xSr_{1-x}TiO_3$ solid solutions (BST) with a well-regulated Ba content. One important BST application is a ferroelectric memory cell capacitor, made by depositing metal layers as electrodes on the top and bottom of thin $Ba_xSr_{1-x}TiO_3$ films [180]. Comprehensive theoretical study of this solid solution combining DFT-LCAO calculations and thermodynamic approach has been performed recently [181].

Meanwhile, $BaTiO_3$ perovskite suffers from degradation, mainly caused by oxygen vacancy migration and redistribution [182]. Solution of this problem requires intensive studies concerning the relaxation processes with O vacancies under different conditions [183, 184].

Despite numerous experimental studies of oxygen vacancies in $BaTiO_3$ [5, 177, 182–185], the number of theoretical simulations of *defective* barium titanate is very limited [5, 132, 143, 149]. The HF and DFT-LCAO study of oxygen vacancies in cubic $BaTiO_3$ perovskite using 34-atom embedded cluster model [132] examined both the charged F^+ and neutral F centers. It was concluded that only the simultaneous association of the two Ti-site acceptors is able to inhibit the formation of a deep e_g state related to a highly symmetrical solution with the electron equally delocalized over the vacancy and both of its nearest Ti neighbors. In this hypothetical situation, conduction band electrons can be localized only at next-neighbor Ti ions; the acceptor-vacancy complex remains a weak perturbation with respect to the cubic site symmetry of the second-neighbor Ti ion. These simulations [132] confirm that an electron, forced to be trapped at a next-neighbor Ti ion, falls into a shallow-gap t_{2g} state indicating the broken symmetry, lying about 1 eV above the e_g state caused by Ti ions nearest to the F center. The estimated ionization energy of this shallow-gap state is ca. 0.1 eV. Nevertheless, the quality of the embedded cluster model used in that study is rather insufficient, to describe properly the covalent bonds broken at the cluster borders.

The INDO periodic 135-atom LUC simulations of oxygen vacancies on the (001) surface were performed for both tetragonal and cubic $BaTiO_3$ phases [143]. It was found that the atomic displacement and charge variation are larger in both phases along

the ferroelectric z-axis {001} than those along the {100} and {010} directions. The F_s center wave function is well localized for the BaO surface termination while it is rather extended in the case of the TiO_2 termination. A lack of periodic ab initio simulations on the O vacancy in $BaTiO_3$ perovskite so far makes comprehensive survey of this system problematic.

As in the case of a regular $Me/SrTiO_3$ (001) interface, the metal films on barium titanate preferably grow in a three-dimensional (3D) mode [186], as islands, when a metal is deposited onto the energetically most stable (001) substrate. Prior to the deposition, the substrates are usually prepared in such a way that predominantly TiO_2-terminated (001) surfaces are expected to occur [187]. So far, only two series of ab initio calculations on periodic models of interfaces between pure cubic $BaTiO_3$ (001) substrate and deposited metals were presented in the literature [180, 188]. In the former study, DFT-PW calculations were performed on the interface between Ta, W, Ir, or Pt metals and the BaO-terminated surface. In our simulations [188], the geometry and adsorption properties of Cu submonolayers on the two possible terminations of a $BaTiO_3$ (001) substrate have been examined using the HF method. In qualitative agreement with previous ab initio simulations on the Me/perovskite surfaces [173–175], we found that the Cu—O bonds on the TiO_2-terminated (001) surface are stronger than those on the BaO-termination. We also observed a certain intermetallic interaction between Cu adatoms and surface Ti ions on the former surface. We have varied copper coverages over the surface oxygen ions and determined that the larger the coverage, the smaller the Cu adsorption energy (per adatom), and the stronger the interatomic interaction inside the metallic overlayer. This explains easier transition to 3D metallic island growth predicted at coverages ≥ 0.5 ML.

4.1.4. $PbTiO_3$

Below 766 K, the crystalline structure of lead titanate changes from simple cubic to tetragonal ferroelectric [150]. Because of a high Curie temperature (220 K) and a large spontaneous polarization [151], piezoelectric, dielectric, and ferroelectric properties of lead titanate make it attractive for a number of applications, such as surface acoustic wave devices, micromechanical and ferroelectric field devices as well as ultrasonic and sonar listening devices [189, 190]. $PbTiO_3$ crystals are also char-

acterized by a nonvolatile, reversible polarization field successfully used in radiation-resistant memories [179]. Moreover, the ferroelectric thin films produced from the $PbTi_xZr_{1-x}O_3$ (PZT) solid solutions were extensively applied and studied since they exhibit high remnant polarizations, suitable coercive fields, and high resistance [142, 151] (see Section 4.3 where lead zirconate is described in more detail).

The wide commercialization of ferroelectric-based devices has been hampered by problems of fatigue, aging, and imprinting [179, 191]. Fatigue and aging affect the lifetime of ferroelectric-based devices and have been extensively investigated; in these processes point defects, including charged oxygen vacancies, play an important role [142]. Indeed, high quality films fabricated by using metal oxide electrodes with a low defect concentration have shown noticeably improved lifetimes and fatigue properties [192].

After cooling below the transition temperature, ferroelectric crystals ($BaTiO_3$ and $PbTiO_3$) adopt a complex microstructure [193] consisting of regions with different orientations of spontaneous polarization (domains). Because of their important role in the performance of numerous ferroelectric devices, these domains, which reduce uncompensated depolarization fields at the surface and release the elastic strain thus reducing the free energy of the crystal, became an object of comprehensive theoretical studies, including the influence of O vacancies [152]. Among various defects, oxygen vacancies are thought to be the most mobile and abundant in perovskite ferroelectrics. The interaction of oxygen vacancies and 180° domain walls in tetragonal $PbTiO_3$ perovskite was estimated [142] using DFT-PW calculations. This study indicates that the vacancies do have a lower formation energy in the domain wall than in the bulk, thus confirming the tendency of these defects to migrate to, and pin, the domain walls. Domain pinning is a major factor in fatigue and can occur as a result of defect *agglomeration* [142]. The pinning effect from a single oxygen vacancy is small.

The DFT-PW calculations of oxygen vacancies in the tetragonal phase of $PbTiO_3$ have examined two types of oxygen vacancies [142], which belong either to: (i) Ti—O—Ti chains along the c axis (parallel to the polarization direction), *hereafter called* O1, or (ii) Ti—O—Ti chains along a- and b-axes normal to the c-axis (O2). Unlike straight cubic-like bonding of O1 (Fig. 5), O2 atoms are bonded to the two Ti atoms in zigzag O—Ti—O chains. Semi-

TABLE III

Comparative analysis of main properties of defective $PbTiO_3$, $PbZrO_3$, and $SrTiO_3$ perovskites obtained in our DFT-LCAO (crystal) calculations for cubic 3×3×3 supercell [18, 141, 147].

Perovskite	Atoms nearest to vacancy	Mulliken charges, e[a] Perfect crystal[b]	Mulliken charges, e[a] Defective crystal	Band gap (eV)	Parameters of defect level (eV) Distance to CB $\Delta\varepsilon_{db\text{-gap}}^{\Gamma}$	Parameters of defect level (eV) Dispersion, δ	Formation energy of F center, $E^{form}(F)$ (eV)
$PbTiO_3$	F center	—	0.85	2.87	0.96	0.21	7.82
	Ti	−2.33	−2.32				
	O	1.23	1.23				
	Pb	−1.34	−1.25				
$PbZrO_3$	F center	—	0.68	3.78	1.71	0.14	7.25
	Zr	−2.07	−2.09				
	O	1.12	1.14				
	Pb	−1.30	−1.17				
$SrTiO_3$	F center	—	1.21	3.63	0.69	0.25	8.74
	Ti	−2.35	−2.34				
	O	1.41	1.42				
	Sr	−1.87	−1.86				

[a] A positive sign means excess of electron density as compared to a neutral atom.
[b] Note that perfect crystals possess Mulliken population of Ti-O, Zr-O, and particularly Pt-O bonds (≤0.4 e each).

empirical periodic INDO calculations [150] show that the positively charged O1 vacancy has the same symmetry as the neutral one, but reveals larger outward displacements of surrounding metal ions. The DFT-PW study [151] focused on the dependence of the calculated formation energy of neutral and charged O vacancies on oxygen partial pressure and crystalline sample growth conditions. Under oxygen-rich conditions, a noticeable increase (from 3 to 5 eV) of the F center formation energy was observed; this is evidently smaller than in $SrTiO_3$ (~7 eV [141]). Moreover, the formation energy of O1 is lower by 0.1 eV than that of O2, which could affect the ferroelectric properties of a defective crystal [151]. The INDO calculations predict the optical absorption energy calculated as the difference of the total self-consistent energies for the ground and excited state of the F center (ΔSCF method) as 2.36 eV [150].

The main shortcoming of periodic simulations described above is insufficient size of the defective supercells, containing from 40 to 80 atoms [142, 150, 151]. In our DFT-LCAO calculations of the F center in a cubic $PbTiO_3$ bulk we used larger, 3×3×3 supercells. In Table III of Section 4.1.4 we compare the main results obtained for similar supercells of cubic $SrTiO_3$, $PbTiO_3$, and $PbZrO_3$. The largest differences between the titanates are: (i) the defect formation energy in $PbTiO_3$ is smaller by ~1 eV

than in $SrTiO_3$ which qualitatively agrees with previous results [151]), (ii) the defect level position $\Delta\varepsilon_{db\text{-gap}}^{\Gamma}$ in $PbTiO_3$ is 0.3 eV deeper with respect to the CB bottom, (iii) the Mulliken charge concentrated inside the O vacancy of $PbTiO_3$ is 0.4 e smaller whereas the nearest Pb neighbor is 0.6 e less ionic, compared to the F center vs. the fully ionic Sr in $SrTiO_3$, respectively (Table III).

4.2. $KNbO_3$ NIOBATE

$KNbO_3$ is widely used in electro-optical and nonlinear optical applications [3, 5]. In particular, reduced samples with O vacancies display fast photorefractive response to short-pulse excitations, which could be used in fast optical correlators. However, the prospects for use of $KNbO_3$ for laser frequency doubling are seriously affected by the presence of unidentified defects responsible for the infrared absorption. This is further complicated, so, since most as-grown samples are nonstoichiometric and contain a considerable amount of vacancies.

First principles calculations of the F centers in $KNbO_3$ were performed already 10 years ago [145] using the DFT method combined with the full-potential (FP) linearized muffin-tin orbitals (LMTO) and relatively small 40 atom supercells. These calculations have shown for the first time that even in the ground state of the F center, the two electrons

from the missing anion are markedly delocalized over the two nearest Nb ions, similarly to titanates discussed in Section 4.1.

The optical absorption of F centers in $KNbO_3$ is a long-debated problem; in particular, whether the 2.7 eV band induced under the electron irradiation could be associated with the F centers [3]. Using the DFT approach, the calculated band gap was found to be considerably smaller than the experimental value of 3.3 eV, thus preventing a correct placing of the F level position within the gap. Thus, another attempt of calculating the optical properties of the neutral F centers and charged F^+ centers in $KNbO_3$ using the semi-empirical INDO periodic LUC method [144] is quite interesting. In this case the band gap was found close to the experimental value and the optical absorption energy was estimated using the ΔSCF method mentioned in the previous Section 4.1.4, which is in principle more accurate than the simple difference of one-electron energies.

The INDO optimized atomic relaxation around the F center indicates an outward shift of the two Nb neighbors with respect to the O vacancy by 7.8%, which is associated with lattice relaxation energy of 1.35 eV [146]. This is close to results of DFT-LMTO calculations, which give 7.0% and 0.5 eV, respectively, as well as to ab initio results for defective $SrTiO_3$.

In the high temperature cubic phase all O ions are equivalent, with arrangement according to C_{4h} local symmetry, whereas in the RT orthorhombic phase there are two types of nonequivalent O ions: O1 and O2 as described in Section 4.1.4. As a result, both the two-electron F center and the one-electron F^+ center in the cubic phase reveal two absorption bands, while in the orthorhombic phase three F-bands are expected.

The semi-empirical INDO calculations predict deep centers with the optical absorption bands around 2.7 eV for both types of F-centers, which needs, however, an independent confirmation by means of ab initio calculations (the only available comparable value of 2.36 eV for $PbTiO_3$ was calculated using the same method). In contrast, the ab initio hybrid calculations on the F center in $SrTiO_3$ predict a much more shallow defect level; however, this difference could be caused by the chemical differences between materials. The INDO approach was also used for modeling of O vacancy migration in $KNbO_3$ [146]. The nonlinear (110) migration path was predicted independently by means of the semi-empirical INDO and empirical SM (shell model) approaches [153] which agree quite well; the diffu-sion barrier for the O vacancy was calculated to be 0.79 and 0.68 eV, respectively [153], qualitatively similar to results obtained for the O vacancy in bulk $SrTiO_3$ (0.4–0.5 eV, see Section 4.1.1).

4.3. $PbZrO_3$ ZIRCONATE

Unlike tetragonal titanate perovskites considered in Section 4.1, the symmetry of the low temperature antiferroelectric $PbZrO_3$ (PZ) phase stable at $T_c \leq 505$ K is orthorhombic ($Pbam$) [194]. This structure is characterized by the antiparallel displacement of Pb atoms in the a–b plane with a subsequent rotation of the ZrO_6 octahedra; the positions of Zr atoms remain largely unchanged. A field-induced ferroelectric phase transition is found feasible in PZ thin films due to a small free energy difference between the ferroelectric ($Pba2$ orthorhombic noncentrosymmetric space group allowing a ferroelectric polarization) and the antiferroelectric phases [195]. Similar to titanates, PZ transforms above T_c to a cubic paraelectric phase.

Because of its antiferroelectric behavior, $PbZrO_3$ is technologically important for applications such as actuators and high-capacity storage devices [196]. As mentioned in Section 4.1.4, PZ is also a parent compound for a series of $PbTi_xZr_{1-x}O_3$ (PZT) solid solutions, which are of high scientific and technological interest for their ferroelectricity and piezoelectricity observed over a wide range of composition [197]. The antiferroelectric PZ thin film heterostructures were found to be radiation-resistant and thus a promising candidate for application in radiation environments [198], including diagnostic materials and bolometers for thermonuclear reactors.

The electronic properties of ideal PZ in the cubic and orthorhombic phases were calculated using the DFT-LDA method [199, 200]. A very small energy difference (0.02 eV) was found between the antiferroelectric and ferroelectric PZ phases, whereas the energy difference between the paraelectric cubic and antiferroelectric orthorhombic (the ground state) phases was calculated to be much larger: 0.27 eV. Comparative DFT-PW calculations on the atomic and electronic structure of PZ, $PbTiO_3$, and $PbTi_{0.5}Zr_{0.5}O_3$ were also performed [201].

Oxygen vacancies could be created in PZ under neutron and ionizing irradiation [198]. Similarly to $PbTiO_3$, these defects make a major impact on the overall performance of the ferroelectric devices based on PZ or PZT [190]. However, no theoretical simulations on PZ containing defects existed until

our recent DFT-LCAO calculations on the atomic and electronic structure of a $3\times3\times3$ supercell of cubic PZ containing *F*-centers [147]. Deformation of oxygen octahedra around the *F* center includes inward and outward displacements of the nearest Pb and Zr atoms, respectively. The nearest lead atoms are shifted towards the vacancy by $\sim$1.5% and accept $\sim$0.13 *e* per Pb atom from the vacancy (vs. $\sim$0.5% outward displacement of each Zr atom and $\sim$0.6 *e* charge donation by it towards the *F* center after break of partly covalent Zr-O bond). This is in contrast to almost complete indifference of the Sr atoms closest to the oxygen vacancy in $SrTiO_3$, which results in substantial difference between the electronic charges accepted by *F* centers in $PbZrO_3$ and $SrTiO_3$ perovskites (0.68 and 1.21 *e*, respectively, as presented in Table III, Section 4.1.4). The magnitude of Pb atom displacement induced by the O vacancy is close to that observed for Pb atoms in the transition from cubic to orthorhombic PZ ($\sim$0.2 Å) [202], which affect its ferroelectric behavior. The formation energy of an O vacancy in cubic PZ is predicted to be 7.25 eV, somewhat smaller than that in cubic $PbTiO_3$ and $SrTiO_3$ perovskites (Table III).

The defect level of the *F* center in cubic PZ lies quite deep, 1.72 eV below the CB bottom (the calculated band gap is 3.78 eV [147] vs. the experimentally measured 3.70 eV [203]). This defect level consists mainly of $6s$ and $6p$ orbitals on the nearst Pb atoms, with a small contribution of Zr $4d$ states. This confirms the charge redistribution based on the Mulliken population analysis predicting considerable charge transfer towards Pb atoms, thus indicating a notable covalency of the Pb—O chemical bond as proposed from the analysis of X-ray diffraction data [204]. This covalency is considerably increased in the orthorhombic phase. Other structural and electronic properties of $PbTiO_3$, $PbZrO_3$ and $SrTiO_3$ ternary oxide bulk are compared in Table III.

5. Summary

In this review article we briefly illustrated the present state-of-the-art in theoretical simulation of defective oxide materials and, in particular, summarized the main achievements of (mostly) first principles modeling of *F* centers in the bulk and on the surface of oxides with different degrees of the chemical bond ionicity. We discussed various periodic and cluster models of defective solids as well as contemporary computational schemes used for their calculations (Section 2). In ionic materials with high atomic coordination, such as Al_2O_3 and MgO (Section 3), classical *F* centers keep almost two electrons in the ground state, which leads to occurrence of deep levels in the band gap. In more covalent ternary oxides $BaTiO_3$, $KNbO_3$ $PbTiO_3$, $PbZrO_3$, and $SrTiO_3$ (Section 4), these electrons tend to be much more delocalized over surrounding metal atoms. For this reason, modeling of point defects in partly covalent and anisotropic ABO_3 perovskites needs use of much larger supercells than in ionic solids.

Numerous simulations of (mostly) neutral oxygen vacancies performed so far dealt with the local atomic structure and electronic density redistribution around defects in their regular lattice sites (mainly after total or partial optimization of the defective structure). Very few studies dealt with defect migration (in bulk and on surface), role of defects in growth mode of deposited metal film on oxide substrates and degradation of the latter. To present reliable atomistic models for theoretical simulations as well as interpretation of the experimental data, the defect theory has to solve the following major problems in the near future: (i) adequate description of charged and excited defects, both periodic and aperiodic; (ii) correct description of band gaps and optical absorption energies, quantitatively close to those obtained in experiments, which needs further improvement of methodology for ab initio simulations; e.g., including a wider implementation of hybrid functionals in the DFT calculations, (iii) treatment of thermodynamic properties of defects in the bulk and on the surface at elevated temperatures.

References

1. Cox, P. A. Transition Metal Oxides: An Introduction to their Electronic Structure and Properties; Clarendon Press: Oxford, UK, 1995.
2. Hayes, W.; Stoneham, A. M. Defects and Defect Processes in Nonmetallic Solids, 2nd ed.; Dover: Mineola, NY, 2004.

3. Kotomin, E. A.; Popov, A. I. Nucl Instrum Methods Phys Res Sect B 1998, 141, 1.

4. Pisani, C., Ed. Quantum-Mechanical *Ab initio* Calculations of the Properties of Crystalline Materials (Springer Lecture Notes in Chemistry, Vol. 67); Springer: Berlin, 1996.

5. Donnerberg, H.-J. Atomic Simulations of Electro-Optical and Magneto-Optical Materials (Springer Tracts in Modern Physics, Vol. 151); Springer: Berlin, 1999.

6. Pacchioni, G. In The Chemical Physics of Solid Surfaces—Oxide Surfaces; Woodruff, D. P., Ed.; Elsevier: Amsterdam, 2001; p 94.

7. Shluger, A. L.; Foster, A. S.; Gavartin, J. L.; Sushko, P. V. In Nano and Giga Challenges in Microelectronics; Greer, J.; Korkin, A.; Labanowski, J., Eds.; Elsevier: North Holland, 2003; p 151.

8. Ellis, D. E.; Warschkow, O. Coord Chem Rev 2003, 238/239, 31.

9. Evarestov, R. A. Phys Status Solidi A 2005, 202, 235.

10. Carrasco, J.; Lopez, N.; Illas, F. Phys Rev Lett 2004, 93, 225502.

11. Lauritsen, J. V.; Foster, A. S.; Olesen, G. H.; Christensen, M. C.; Kühnle, A.; Helveg, S.; Rostrup-Nielsen, J. R.; Clausen, B. S.; Reichling, M.; Besenbacher, F. Nanotechnology 2006, 17, 3436.

12. Muller, D. A.; Nakagawa, N.; Ohtomo, A.; Grazul, J. L.; Hwang, H. Y. Nature 2004, 430, 657.

13. (a) Makov, G.; Payne, M. C. Phys Rev B 1995, 51, 4014; (b) Makov, G.; Payne, M. C. Phys Rev B 1996, 53, 15513.

14. Kantorovich, L. N. Phys Rev B 1999, 60, 15476.

15. Onida, G.; Reining, L.; Rubio, A. Rev Mod Phys 2002, 74, 601.

16. Kantorovich, L. N. Int J Quantum Chem 2000, 78, 306.

17. Klüner, T.; Govind, N.; Wang, Y. A.; Carter, E. A. J Chem Phys 2002, 116, 42.

18. Evarestov, R. A.; Kotomin, E. A.; Zhukovskii, Y. F. Int J Quantum Chem 2006, 106, 2173.

19. Fuks, D.; Zhukovskii, Y. F.; Kotomin, E. A.; Ellis, D. E. Surf Sci 2006, 600, L99.

20. Evarestov, R. A. Quantum Chemistry of Solids. The LCAO First Principles Treatment of Crystals (Springer Series in Solid State Sciences, Vol. 153); Springer: Heidelberg, 2007.

21. Deák, P. Phys Status Solidi B 2000, 217, 9.

22. Pisani, C.; Dovesi, R.; Roetti, C.; Causá, M.; Casassa, S.; Saunders, V. R. Int J Quantum Chem 2000, 77, 1032.

23. Pisani, C.; Birkenheuer, U.; Cora, F.; Nada, R.; Casassa, S. EMBED-96 User's Manual; University of Turin: Italy, 1996.

24. Bredow, T.; Evarestov, R. A.; Jug, K. Phys Status Solidi B 2000, 222, 495.

25. Stefanovich, E. V.; Shidlovskaya, E. K.; Shluger, A. L.; Zakharov, M. K. Phys Status Solidi B 1990, 160, 529.

26. Bredow, T.; Geudtner, G.; Jug, K. J Comput Chem 2001, 22, 861.

27. Evarestov, R. A.; Smirnov, V. P. Site Symmetry in Crystals: Theory and Applications (Springer Series in Solid State Sciences, Vol. 108); Springer: New York, 1997.

28. Evarestov, R. A.; Piskunov, S.; Kotomin, E. A.; Borstel, G.; Phys Rev B 2003, 67, 064101.

29. Evarestov, R. A.; Bandura, A. V. Int J Quantum Chem 2004, 100, 452.

30. Monkhorst, H. J.; Pack, J. D. Phys Rev B 1976, 13, 5188.

31. Perdew, J. P.; Burke, K.; Ernzerhof, M. Phys Rev Lett 1996, 77, 3865.

32. Becke, A. D. Phys Rev A 1988, 38, 3098.

33. Lee, C.; Yang, W.; Parr, R. G. Phys Rev B 1988, 37, 785.

34. Perdew, J. P.; Wang, Y. Phys Rev B 1992, 45, 13244.

35. Tao, J.; Perdew, J. P.; Staroverov, V. N.; Scuseria, G. E. Phys Rev B 2004, 69, 075102.

36. Perdew, J. P.; Wang, Y. Phys Rev B 1986, 33, 8800.

37. Saunders, V. R.; Dovesi, R.; Roetti, C.; Orlando, R.; Zicovich-Wilson, C. M.; Harrison, N. M.; Doll, K.; Civalleri, B.; Bush, I. J.; D'Arco, P.; Llunell, M. *CRYSTAL-2003* User Manual; University of Turin: Italy, 2003.

38. Rohrbach, A.; Hafner, J.; Kresse, G. J Phys: Condens Matter 2003, 15, 979.

39. Kresse, G.; Hafner, J. *VASP* Guide; University of Vienna: Austria, 2003.

40. Paier, J.; Hirschl, R.; Marsman, M.; Kresse, G.; J Chem Phys 2005, 122, 234102.

41. Heyd, J.; Scuseria, G. E.; Ernzerhof, M.; J Chem Phys 2003, 118, 8207.

42. Corá, F.; Alfredsson, M.; Mallia, G.; Midlemiss, D.; Mackrodt, W. C.; Dovesi, R.; Orlando, R. In Principles and Applications of Density Functional Theory in Inorganic Chemistry II; Mingos, D. M. P., Ed.; Springer Series in Structure and Bonding, Vol. 113; Springer: Berlin, 2004.

43. Kantorovich, L. N.; Holender, J. M.; Gillan, M. J. Surf Sci 1995, 343, 221.

44. Zhukovskii, Y. F.; Kotomin, E. A.; Jacobs, P. W. M.; Stoneham, A. M. Phys Rev Lett 2000, 84, 1256.

45. Carrasco, J.; Lopez, N.; Illas, F.; Freund, H.-J. J Chem Phys 2006, 125, 074711.

46. Scorza, E.; Birkenheuer, U.; Pisani, C. J Chem Phys 1997, 107, 9645.

47. Sushko, P. V.; Shluger, A. L.; Catlow, C. R. A.; Surf Sci 2000, 450, 153.

48. Matveev, A. V.; Neyman, K. M.; Yudanov, I. V.; Rösch, N. Surf Sci 1999, 426, 123.

49. Nasluzov, V. A.; Rivanenkov, V. V.; Gordienko, A. B.; Neyman, K. M.; Birkenheuer, U.; Rösch, N. J Chem Phys 2001, 115, 8157.

50. (a) Ferrari, A. M.; Pacchioni, G. J Phys Chem 1995, 99, 17010; (b) Ferrari, A. M.; Pacchioni, G. J Phys Chem 1996, 100, 9032.

51. Sousa, B.; Illas, F. J Chem Phys 2001, 115, 1435.

52. Eglitis, R. I.; Kuklja, M. M.; Kotomin, E. A.; Stashans, A.; Popov, A. I. Comput Mater Sci 1996, 5, 298.

53. Ahlswede, B.; Homann, T.; Jug, K. Surf Sci 2000, 445, 49.

54. Kappers, L. A.; Kroes, R. L.; Hensely, E. B. Phys Rev B 1970, 1, 4151.

55. Popov, A. I.; Monge, M. A.; González, R.; Chen, Y.; Kotomin, E. A. Solid State Commun 2001, 118, 163.

56. Whited, R. C.; Flaten, C. J.; Walker, W. C. Solid State Commun 1973, 13, 1903.

57. Tasker, P. W. J Phys C: Solid State Phys 1979, 12, 4977.

58. Abriou, D.; Creuzet, F.; Jupille, J. Surf Sci 1996, 352, 499.

59. Subramanian, A.; Marks, L. D.; Warschkow, O.; Ellis, D. E. Phys Rev Lett 2004, 92, 026101.

60. Watson, G. W.; Kelsey, E. T.; de Leeuw, N. H.; Harris, D. J.; Parker, S. C. J Chem Soc Faraday Trans 1996, 92, 433.

61. Zhukovskii, Y. F.; Kotomin, E. A.; Jacobs, P. W. M.; Stoneham, A. M.; Harding, J. H. Surf Sci 1999, 441, 373.

62. Zhukovskii, Y. F.; Kotomin, E. A.; Borstel, G. Vacuum 2004, 74, 235.

63. Kantorovich, L. N.; Shluger, A. L.; Sushko, P. V.; Günster, J.; Goodman, D. W.; Stracke, P.; Kempter, V. Faraday Discuss 1999, 114, 173.

64. Campbell, C. T. Surf Sci Rep 1997, 27, 1.

65. Campbell, C. T.; Parker, S. C.; Starr, D. E. Science 2002, 298, 811.

66. Renauld, G.; Lazzari, R.; Revenant, C.; Barbier, A.; Noblet, M.; Ulrich, O.; Leroy, F.; Jupille, J.; Borensztein, Y.; Henry, C. R.; Deville, J.-P.; Scheurer, F.; Mane-Mane, J.; Fruchartet, O. Science 2003, 300, 1416.

67. Meyerheim, H. L.; Popescu, R.; Kirschner, J.; Jedrecy, N.; Sauvage-Simkin, M.; Heinrich, B.; Pinchaux, R. Phys Rev Lett 2001, 87, 076102.

68. Hong, T.; Smith, J. R.; Srolovitz, D. J. Acta Metall Mater 1995, 43, 2721.

69. Heifets, E.; Zhukovskii, Y. F.; Kotomin, E. A.; Causá, M. Chem Phys Lett 1998, 283, 395.

70. (a) Goniakowski, J. Phys Rev B 1998, 57, 1935; (b) Goniakowski, J. Phys Rev B 1998, 58, 1189.

71. Butler, W. H.; Zhang, X.-G.; Schulthess, T. C.; MacLaren, J. M. Phys Rev B 2001, 63, 054416.

72. Markovits, A.; Paniagua, J. C.; Lopez, N.; Minot, C.; Illas, F. Phys Rev B 2003, 67, 115417.

73. Zhukovskii, Y. F.; Kotomin, E. A.; Fuks, D.; Dorfman, S.; Stoneham, A. M.; Borstel, G. J Phys: Condens Matter 2004, 16, 4881.

74. Zhukovskii, Y. F.; Kotomin, E. A.; Fuks, D.; Dorfman, S. Superlattices Microstruct 2004, 36, 63.

75. Musolino, V.; Selloni, A.; Car, R. Phys Rev Lett 1999, 83, 3242.

76. Ferrari, A. M.; Xiao, C.; Neyman, K. M.; Pacchioni, G.; Rösch, N. Phys Chem Chem Phys 1999, 1, 4655.

77. Moseler, M.; Häkkinen, H.; Landman, U. Phys Rev Lett 2002, 89, 176103.

78. Grönbeck, H.; Broqvist, P. J Chem Phys 2003, 119, 3896.

79. Sljivancanin, Z.; Pasquarello, A. Phys Rev Lett 2003, 90, 247202.

80. Giordano, L.; di Valentin, C.; Goniakowski, J.; Pacchioni, G. Phys Rev Lett 2004, 92, 096105.

81. Benedek, R.; Alavi, A.; Seidman, D. N.; Yang, L. H.; Muller, D. A.; Woodward, C. Phys Rev Lett 2000, 84, 3362.

82. Sutton, A. P.; Balluffi, R. W. Interfaces in Crystalline Solids; Oxford University Press: New York, 1996.

83. Duffy, D. M.; Harding, J. H.; Stoneham, A. M. J Appl Phys 1994, 76, 2791.

84. Purton, J.; Parker, S. C.; Bullett, D. W. J Phys: Condens Matter 1997, 9, 5709.

85. Fuks, D.; Dorfman, S.; Zhukovskii, Y. F.; Kotomin, E. A.; Stoneham, A. M. Surf Sci 2002, 499, 24.

86. Fuks, D.; Kotomin, E. A.; Zhukovskii, Y. F.; Stoneham, A. M. Phys Rev B 2006, 74, 115418.

87. (a) Bogicevic, A.; Jennison, D. R. Surf Sci 1999, 437, L741; (b) Bogicevic, A.; Jennison, D. R. Surf Sci 2002, 515, L481.

88. Zhukovskii, Y. F.; Kotomin, E. A.; Jacobs, P. W. M.; Stoneham, A. M.; Harding, J. H. J Phys: Condens Matter 2000, 12, 55.

89. Yang, Z.; Wu, R.; Zhang, Q.; Goodman, D. W. Phys Rev 2002, 65, 155407.

90. Lopez, N.; Valeri, S. Phys Rev B 2004, 70, 125428.

91. Zhukovskii, Y. F.; Kotomin, E. A. Phys Status Solidi C 2005, 2, 347.

92. Neyman, K. M.; Inntam, C.; Matveev, A. V.; Nasluzov, V. A.; Rösch, N. J Am Chem Soc 2005, 127, 11652.

93. Brune, H. Surf Sci Rep 1998, 31, 121.

94. Venables, J. Introduction to Surface and Thin Film Processes; University Press: Cambridge, 2000.

95. Zhukovskii, Y. F.; Fuks, D.; Kotomin, E. A.; Ellis, D. E. Nucl Instrum Methods Phys Res Sect B 2007, 255, 219.

96. Cai, S.-H.; Rashkeev, S. N.; Pantelides, S. T.; Sohlberg, K. Phys Rev Lett 2002, 89, 235501.

97. Wolverton, C.; Hass, K. C. Phys Rev B 2001, 63, 024102.

98. Wefers, K.; Misra, C. Oxides and hydroxides of aluminum; Alcoa Laboratories: Pittsburgh, 1987. Alcoa Technical Paper No. 19.

99. Wyckoff, R. W. G. Crystal Structures, 2nd ed.; Interscience: New York, 1964; Vol. 2.

100. Xu, Y. N.; Gu, Z. Q.; Zhong, X. F.; Ching, W. Y. Phys Rev B 1997, 56, 7277.

101. Tanaka, I.; Tatsumi, K.; Nakano, M.; Adachi, H.; Oba, F. J Am Ceram Soc 2002, 85, 68.

102. Matsunaga, K.; Tanaka, T.; Yamamoto, T.; Ikuhara, Y. Phys Rev B 2003, 68, 085110.

103. Carrasco, J.; Gomes, J. R. B.; Illas, F. Phys Rev B 2004, 69, 064116.

104. Carrasco, J.; Lopez, N.; Sousa, C.; Illas, F. Phys Rev B 2005, 72, 054109.

105. Stashans, A.; Kotomin, E. A.; Calais, J.-L. Phys Rev B 1994, 49, 14854.

106. Janetzko, F.; Evarestov, R. A.; Bredow, T.; Jug, K. Phys Status Solidi B 2004, 241, 1032.

107. Frisch, M. J.; Trucks, G. W.; Schlegel, H. B.; Scuseria, G. E.; Robb, M. A.; Cheeseman, J. R.; Montgomery, J. A., Jr.; Vreven, T.; Kudin, K. N.; Burant, J. C.; Millam, J. M.; Iyengar, S. S.; Tomasi, J.; Barone, V.; Mennucci, B.; Cossi, M.; Scalmani, G.; Rega, N.; Petersson, G. A.; Nakatsuji, H.; Hada, M.; Ehara, M.; Toyota, K.; Fukuda, R.; Hasegawa, J.; Ishida, M.; Nakajima, T.; Honda, Y.; Kitao, O.; Nakai, H.; Klene, M.; Li, X.; Knox, J. E.; Hratchian, H. P.; Cross, J. B.; Bakken, V.; Adamo, C.; Jaramillo, J.; Gomperts, R.; Stratmann, R. E.; Yazyev, O.; Austin, A. J.; Cammi, R.; Pomelli, C.; Ochterski, J. W.; Ayala, P. Y.; Morokuma, K.; Voth, G. A.; Salvador, P.; Dannenberg, J. J.; Zakrzewski, V. G.; Dapprich, S.; Daniels, A. D.; Strain, M. C.; Farkas, O.; Malick, D. K.; Rabuck, A. D.; Raghavachari, K.; Foresman, J. B.; Ortiz, J. V.; Cui, Q.; Baboul, A. G.; Clifford, S.; Cioslowski, J.; Stefanov, B. B.; Liu, G.; Liashenko, A.; Piskorz, P.; Komaromi, I.; Martin, R. L.; Fox, D. J.; Keith, T.; Al-Laham, M. A.; Peng, C. Y.; Nanyakkara, A.; Challacombe, M.; Gill,

P. M. W.; Johnson, B.; Chen, W.; Wong, M. W.; Gonzalez, C.; Pople, J. A. GAUSSIAN-2003, Revision B 4; Pittsburgh, 2003.

108. Harding, J. H.; Atkinson, K. J. W.; Grimes, R. W. J Am Ceram Soc 2003, 86, 554.

109. French, R. H. J Am Ceram Soc 1990, 73, 477.

110. Muscat, J.; Wander, A.; Harrison, N. M. Chem Phys Lett 2001, 342, 397.

111. Sousa, C.; Illas, F.; Pacchioni, G. J Chem Phys 1993, 99, 6818.

112. Zhang, S. B.; Northrup, J. E. Phys Rev Lett 1991, 67, 2339.

113. Jacobs, P. W. M.; Kotomin, E. A. Philos Mag A 1993, 68, 695.

114. Heuer, A. H.; Lagerloff, K. P. D. Philos Mag Lett 1999, 79, 619.

115. Evans, B. D.; J Nucl Mater 1995, 219, 202.

116. Baxter, R.; Reinhardt, P.; Lopez, N.; Illas, F. Surf Sci 2000, 445, 448.

117. Guo, J.; Ellis, D. E.; Lam, D. J. Phys Rev B 1992, 45, 13647.

118. Puchin, V. E.; Gale, J. D.; Shluger, A. L.; Kotomin, E. A.; Günster, J.; Brause, M.; Kempter, V. Surf Sci 1997, 370, 190.

119. Zhukovskii, Y. F.; Kotomin, E. A.; Herschend, B.; Hermansson, K.; Jacobs, P. W. M. Surf Sci 2002, 513, 343.

120. Lodziana, Z.; Norskøv, J. K.; Stoltze, P. J Chem Phys 2003, 118, 11179.

121. Verdozzi, C.; Jennison, D. R.; Schultz, P. A.; Sears, M. P. Phys Rev Lett 1999, 82, 799.

122. Batyrev, I. G.; Alavi, A.; Finnis, M. W.; Deutsch, T. Phys Rev Lett 1999, 82, 1510.

123. Zhang, W.; Smith, J. R. Phys Rev B 2000, 61, 16883.

124. Batyrev, I. G.; Kleinman, L. Phys Rev B 2001, 64, 033410.

125. (a) Gomes, J. R. B.; Illas, F.; Hernandez, N. C.; Marquez, A.; Sanz, J. F. Phys Rev B 2002, 65, 125414; (b) Gomes, J. R. B.; Illas, F.; Hernandez, N. C.; Sanz, J. F.; Wander, A.; Harrison, N. M. J Chem Phys 2002, 116, 1684.

126. Mattsson, A. E.; Jennison, D. R. Surf Sci 2002, 520, L611.

127. Rashkeev, S. N.; Sohlberg, K.; Glazoff, M. V.; Novak, J.; Pennycook, S. J.; Pantelides, S. T. Phys Rev B 2003, 67, 115414.

128. Tanaka, S.; Yang, R.; Kohyama, M.; Sasaki, T.; Matsunaga, K.; Ikuhara, Y. Mater Trans 2004, 45, 1973.

129. Sanz, J. F.; Hernandez, N. C. Phys Rev Lett 2005, 94, 016104.

130. Zhukovskii, Y. F.; Kotomin, E. A.; Mastrikov, Y.; Maier, J. Comput Mater Sci 2005, 33, 276.

131. Fang, Z.; Terakura, K. Surf Sci 2000, 470, L75.

132. Donnerberg, H.; Birkholz, A. J Phys: Condens Matter 2000, 12, 8239.

133. Stashans, A.; Vargas, F. Mater Lett 2001, 50, 145.

134. Astala, R.; Bristowe, P. D. Modell Simul Mater Sci Eng 2001, 9, 415.

135. Stashans, A.; Erazo, F.; Ortiz, J.; Valverde, P. Philos Mag B 2001, 81, 1977.

136. Ricci, D.; Bano, G.; Pacchioni, G.; Illas, F. Phys Rev B 2003, 68, 224105.

137. Tanaka, T.; Matsunaga, K.; Ikuhara, Y.; Yamamoto, T. Phys Rev B 2003, 68, 205213.

138. Buban, J. P.; Iddir, H.; Ogut, S. Phys Rev B 2004, 69, 180102(R).

139. Luo, W.; Duan, W.; Louie, S. G.; Cohen, M. L. Phys Rev B 2004, 70, 214109.

140. Carrasco, J.; Illas, F.; Lopez, N.; Kotomin, E. A.; Zhukovskii, Y. F.; Piskunov, S.; Maier, J.; Hermansson, K.; Phys Status Solidi C 2005, 2, 153.

141. Carrasco, J.; Illas, F.; Lopez, N.; Kotomin, E. A.; Zhukovskii, Y. F.; Evarestov, R. A.; Mastrikov, Y.; Piskunov, S.; Maier, J. Phys Rev B 2006, 73, 064106.

142. Park, C. H.; Chadi, D. J. Phys Rev B 1998, 57, R13961.

143. Duque, C.; Stashans, A. Mater Lett 2003, 57, 3954.

144. Kotomin, E. A.; Eglitis, R. I.; Popov, A. I.; J Phys: Condens Matter 1997, 9, L315.

145. Eglitis, R. I.; Christensen, N. E.; Postnikov, A. I.; Kotomin, E. A.; Borstel, G. Phys Rev B 1997, 55, 8599.

146. Eglitis, R. I.; Kotomin, E. A.; Borstel, G. Phys Status Solidi C 2005, 2, 113.

147. Piskunov, S.; Gopeyenko, A.; Kotomin, E. A.; Zhukovskii, Y. F.; Ellis, D. E. Comput Mater Sci 2007 (in press).

148. Stashans, A.; Serrano, S. Surf Sci 2002, 497, 285.

149. Stashans, A. Int J Nanotechnol 2004, 1, 399.

150. Stashans, A.; Serrano, S.; Medina, P. Phys B 2006, 381, 82.

151. Zhang, Z.; Wu, P.; Lu, L.; Shu, C. Appl Phys Lett 2006, 88, 142902.

152. He, L.; Vanderbilt, D. Phys Rev B 2003, 68, 134103.

153. Jacobs, P. W. M.; Kotomin, E. A.; Eglitis, R. I. J Phys: Condens Matter 2000, 12, 569.

154. Heifets, E.; Kotomin, E. A.; Trepakov, V. A. J Phys: Condens Matter 2006, 18, 4845.

155. Van Benthem, K.; Elsässer, C.; French, R. H. J Appl Phys 2001, 90, 6156.

156. Moos, R.; Haerdtl, K.-H. J Am Ceram Soc 1997, 80, 2549.

157. Denk, I.; Munch, W.; Maier, J. J Am Ceram Soc 1995, 78, 3265.

158. Crawford, J.; Jacobs, P. W. M. J Solid State Chem 1999, 144, 423.

159. Usvyat, D. E.; Evarestov, R. A.; Smirnov, V. P. Int J Quantum Chem 2004, 100, 352.

160. Hünnefeld, H.; Niemöller, T.; Schneider, J. R.; Rütt, U.; Rodewald, S.; Fleig, J.; Shirane, G. Phys Rev B 2002, 66, 014113.

161. Heifets, E.; Eglitis, R. I.; Kotomin, E. A.; Maier, J.; Borstel, G. Phys Rev B 2001, 64, 23417.

162. Heifets, E.; Eglitis, R. I.; Kotomin, E. A.; Maier, J.; Borstel, G. Surf Sci 2002, 513, 211.

163. Piskunov, S.; Heifets, E.; Kotomin, E. A.; Maier, J.; Eglitis, R. I.; Borstel, G. Surf Sci 2005, 575, 75.

164. Padilla, J.; Vanderbilt, D. Surf Sci 1998, 418, 64.

165. Cheng, C.; Kunc, K.; Lee, M. H. Phys Rev B 2000, 62, 10409.

166. Xue, X. Y.; Wang, C. L.; Zhong, W. L. Surf Sci 2004, 550, 73.

167. Mackrodt, M. C. Phys Chem Mater 1988, 15, 228.

168. Heifets, E.; Kotomin, E. A.; Maier, J. Surf Sci 2000, 462, 462.

169. (a) Kazimirov, A.; Goodner, D. M.; Bedzyk, M. J.; Bai, J.; Hubbard, C. R. Surf Sci 2001, 492, L711; (b) Koster, G.; Rijnders, G.; Blank, D. H. A.; Rogalla, H. Phys C 2000, 339, 215; (c) Gonzalez, M. S. M.; Aguirre, M. H.; Moran, E.; Alario-Franco, M. A.; Perez-Dieste, V.; Avila, J.; Asensio, M. C. Solid State Sci 2000, 2, 519.

170. Erdman, N.; Poeppelmeier, K. R.; Asta, M.; Warschkow, O.; Ellis, D. E.; Marks, L. D. Nature 2002, 419, 55.

171. Heifets, E.; Piskunov, S.; Kotomin, E. A.; Zhukovskii, Y. F.; Ellis, D. E. Phys Rev B 2007, 75, 115417.

172. Bando, H.; Aiura, Y.; Haruyama, Y.; Shimizu, T.; Nishihara, Y. J Vac Sci Technol B 1995, 13, 1150.

173. Ochs, T.; Kostmeier, S.; Elsässer, C. Integr Ferroelectrics 2001, 32, 959.

174. Ochs, T.; Elsässer, C. Z Metallkd 2002, 93, 406.

175. Asthagiri, A.; Sholl, D. S. J Chem Phys 2002, 116, 9914.

176. Wagner, T.; Richter, G.; Rühle, M. J Appl Phys 2001, 89, 2602.

177. Zhong, W.; Vanderbilt, D.; Rabe, K. M. Phys Rev Lett 1994, 73, 1861.

178. Lines, M. E.; Glass, A. M. Principles and Applications of Ferroelectrics and Related Materials; Clarendon Press: Oxford, UK, 1997.

179. Scott, J. F.; Paz de Araujo, C. A. Science 1989, 246, 1400.

180. Rao, F.; Kim, M.; Freeman, A. J.; Tang, S.; Anthony, M. Phys Rev B 1997, 55, 13951.

181. Fuks, D.; Dorfman, S.; Piskunov, S.; Kotomin, E. A. Phys Rev B 2005, 71, 014111.

182. Chen, L.; Xiong, X. M.; Meng, H.; Lu, P.; Zhang, J. X. Appl Phys Lett 2006, 89, 071916.

183. Yang, G. Y.; Dickey, E. C.; Randall, C. A. J Appl Phys 2003, 94, 5990.

184. Woodward, D. I.; Reaney, I. M.; Yang, G. Y.; Dickey, E. C.; Randall, C. A. Appl Phys Lett 2004, 84, 4650.

185. Xiao, Y.; Shenoy, V. B.; Bhattacharya, K. Phys Rev Lett 2005, 95, 247603.

186. Hill, D. M.; Meyer, H. M., III; Weaver, J. H. J Appl Phys 1989, 65, 4943.

187. Kawasaki, M.; Takahashi, K.; Maeda, T.; Tsuchiya, R.; Shinohara, M.; Ishiyama, O.; Yonezawa, T.; Yoshimoto, M.; Koinuma, H. Science 1994, 266, 1540.

188. Zhukovskii, Y. F.; Piskunov, S.; Kotomin, E. A.; Sychev, O.; Borstel, G. Microelectron Eng 2005, 81, 467.

189. Haertling, G. H. J Vac Sci Technol A 1991, 9, 414.

190. Ahn, C. H.; Hammond, R. H.; Geballe, T. H.; Beasley, M. R.; Triscone, J.-M.; Decroux, M.; Fischer, O.; Antognazza, L.; Char, K. Appl Phys Lett 1997, 70, 206.

191. Warren, W. L.; Dimos, D.; Waser, R. M. Mater Res Bull 1996, 21, 40.

192. Nakamura, T.; Nakao, Y.; Kamisawa, A.; Takasu, H. Appl Phys Lett 1994, 65, 1522.

193. Meyer, B.; Vanderbilt, D. Phys Rev B 2002, 65, 104111.

194. (a) Fujishita, H. Ferroelectrics 2002, 266, 27; (b) Fujishita, H.; Ishikawa, Y.; Tanaka, S.; Ogawaguchi, A.; Katano, S. J Phys Soc Jpn 2003, 72, 1426.

195. Bharadwaja, S. S. N.; Krupanidhi, S. B. J Appl Phys 2001, 89, 4541.

196. Yamakawa, K.; Trolier-McKinstry, S.; Dougherty, J. P.; Krupanidhi, S. B. Appl Phys Lett 1995, 67, 1014.

197. Seveno, R.; Gundel, H. W.; Seifert, S. Appl Phys Lett 2001, 79, 4204.

198. Bittner, R.; Humer, K.; Weber, H. W.; Kundzins, K.; Sternberg, A.; Lesnyh, D. A.; Kulikov, D. V.; Trushin, Y. V. J Appl Phys 2004, 96, 3239.

199. Singh, D. J. Phys Rev B 1995, 52, 12559.

200. Johannes, M. D.; Singh, D. J. Phys Rev B 2005, 71, 212101.

201. Rodriguez, J. A.; Etxeberria, A.; González, L.; Maiti, A. J Chem Phys 2002, 117, 2699.

202. Sawaguchi, E. Ferroelectrics 2002, 266, 341.

203. Robertson, J. J Vac Sci Technol B 2000, 18, 1785.

204. Aoyagi, S.; Kuroiwa, Y.; Sawada, A.; Tanaka, H.; Harada, J.; Nishibori, E.; Takata, M.; Sakata, M. J Phys Soc Jpn 2002, 71, 2353.